arXiv:hep-ex/0608002v2 20 Sep 2006

Measurement of *CP*-Violating Asymmetries in $B^0 \to (\rho\pi)^0$ Using a Time-Dependent Dalitz Plot Analysis

The *BABAR* Collaboration

October 13, 2018

Abstract

We report a measurement of *CP*-violating asymmetries in $B^0 \to (\rho\pi)^0 \to \pi^+\pi^-\pi^0$ decays using a time-dependent Dalitz plot analysis. The results are obtained from a data sample of 347 million $\Upsilon(4S) \to B\overline{B}$ decays, collected by the *BABAR* detector at the PEP-II asymmetric-energy B Factory at SLAC. We measure 26 coefficients of the bilinear form factor terms occurring in the time-dependent decay rate of the B^0 meson and derive the physically relevant quantities from these coefficients. In particular we find a three standard deviation evidence of direct *CP*-violation in the $B^0 \to \rho^\pm\pi^\mp$ decays, with systematic uncertainties included. We also achieve a constraint of the angle α of the Unitarity Triangle. All results presented are preliminary.

The *BABAR* Collaboration,

B. Aubert, R. Barate, M. Bona, D. Boutigny, F. Couderc, Y. Karyotakis, J. P. Lees, V. Poireau,
V. Tisserand, A. Zghiche

Laboratoire de Physique des Particules, IN2P3/CNRS et Université de Savoie, F-74941 Annecy-Le-Vieux,
France

E. Grauges

Universitat de Barcelona, Facultat de Fisica, Departament ECM, E-08028 Barcelona, Spain

A. Palano

Università di Bari, Dipartimento di Fisica and INFN, I-70126 Bari, Italy

J. C. Chen, N. D. Qi, G. Rong, P. Wang, Y. S. Zhu

Institute of High Energy Physics, Beijing 100039, China

G. Eigen, I. Ofte, B. Stugu

University of Bergen, Institute of Physics, N-5007 Bergen, Norway

G. S. Abrams, M. Battaglia, D. N. Brown, J. Button-Shafer, R. N. Cahn, E. Charles, M. S. Gill,
Y. Groysman, R. G. Jacobsen, J. A. Kadyk, L. T. Kerth, Yu. G. Kolomensky, G. Kukartsev, G. Lynch,
L. M. Mir, T. J. Orimoto, M. Pripstein, N. A. Roe, M. T. Ronan, W. A. Wenzel

Lawrence Berkeley National Laboratory and University of California, Berkeley, California 94720, USA

P. del Amo Sanchez, M. Barrett, K. E. Ford, A. J. Hart, T. J. Harrison, C. M. Hawkes, S. E. Morgan,
A. T. Watson

University of Birmingham, Birmingham, B15 2TT, United Kingdom

T. Held, H. Koch, B. Lewandowski, M. Pelizaeus, K. Peters, T. Schroeder, M. Steinke

Ruhr Universität Bochum, Institut für Experimentalphysik 1, D-44780 Bochum, Germany

J. T. Boyd, J. P. Burke, W. N. Cottingham, D. Walker

University of Bristol, Bristol BS8 1TL, United Kingdom

D. J. Asgeirsson, T. Cuhadar-Donszelmann, B. G. Fulsom, C. Hearty, N. S. Knecht, T. S. Mattison,
J. A. McKenna

University of British Columbia, Vancouver, British Columbia, Canada V6T 1Z1

A. Khan, P. Kyberd, M. Saleem, D. J. Sherwood, L. Teodorescu

Brunel University, Uxbridge, Middlesex UB8 3PH, United Kingdom

V. E. Blinov, A. D. Bukin, V. P. Druzhinin, V. B. Golubev, A. P. Onuchin, S. I. Serednyakov,
Yu. I. Skovpen, E. P. Solodov, K. Yu Todyshev

Budker Institute of Nuclear Physics, Novosibirsk 630090, Russia

D. S. Best, M. Bondioli, M. Bruinsma, M. Chao, S. Curry, I. Eschrich, D. Kirkby, A. J. Lankford, P. Lund,
M. Mandelkern, R. K. Mommsen, W. Roethel, D. P. Stoker

University of California at Irvine, Irvine, California 92697, USA

S. Abachi, C. Buchanan

University of California at Los Angeles, Los Angeles, California 90024, USA

2

S. D. Foulkes, J. W. Gary, O. Long, B. C. Shen, K. Wang, L. Zhang

University of California at Riverside, Riverside, California 92521, USA

H. K. Hadavand, E. J. Hill, H. P. Paar, S. Rahatlou, V. Sharma

University of California at San Diego, La Jolla, California 92093, USA

J. W. Berryhill, C. Campagnari, A. Cunha, B. Dahmes, T. M. Hong, D. Kovalskyi, J. D. Richman

University of California at Santa Barbara, Santa Barbara, California 93106, USA

T. W. Beck, A. M. Eisner, C. J. Flacco, C. A. Heusch, J. Kroseberg, W. S. Lockman, G. Nesom, T. Schalk,
B. A. Schumm, A. Seiden, P. Spradlin, D. C. Williams, M. G. Wilson

University of California at Santa Cruz, Institute for Particle Physics, Santa Cruz, California 95064, USA

J. Albert, E. Chen, A. Dvoretskii, F. Fang, D. G. Hitlin, I. Narsky, T. Piatenko, F. C. Porter, A. Ryd,
A. Samuel

California Institute of Technology, Pasadena, California 91125, USA

G. Mancinelli, B. T. Meadows, K. Mishra, M. D. Sokoloff

University of Cincinnati, Cincinnati, Ohio 45221, USA

F. Blanc, P. C. Bloom, S. Chen, W. T. Ford, J. F. Hirschauer, A. Kreisel, M. Nagel, U. Nauenberg,
A. Olivas, W. O. Ruddick, J. G. Smith, K. A. Ulmer, S. R. Wagner, J. Zhang

University of Colorado, Boulder, Colorado 80309, USA

A. Chen, E. A. Eckhart, A. Soffer, W. H. Toki, R. J. Wilson, F. Winklmeier, Q. Zeng

Colorado State University, Fort Collins, Colorado 80523, USA

D. D. Altenburg, E. Feltresi, A. Hauke, H. Jasper, J. Merkel, A. Petzold, B. Spaan

Universität Dortmund, Institut für Physik, D-44221 Dortmund, Germany

T. Brandt, V. Klose, H. M. Lacker, W. F. Mader, R. Nogowski, J. Schubert, K. R. Schubert, R. Schwierz,
J. E. Sundermann, A. Volk

Technische Universität Dresden, Institut für Kern- und Teilchenphysik, D-01062 Dresden, Germany

D. Bernard, G. R. Bonneaud, E. Latour, Ch. Thiebaux, M. Verderi

Laboratoire Leprince-Ringuet, CNRS/IN2P3, Ecole Polytechnique, F-91128 Palaiseau, France

P. J. Clark, W. Gradl, F. Muheim, S. Playfer, A. I. Robertson, Y. Xie

University of Edinburgh, Edinburgh EH9 3JZ, United Kingdom

M. Andreotti, D. Bettoni, C. Bozzi, R. Calabrese, G. Cibinetto, E. Luppi, M. Negrini, A. Petrella,
L. Piemontese, E. Prencipe

Università di Ferrara, Dipartimento di Fisica and INFN, I-44100 Ferrara, Italy

F. Anulli, R. Baldini-Ferroli, A. Calcaterra, R. de Sangro, G. Finocchiaro, S. Pacetti, P. Patteri,
I. M. Peruzzi,[1] M. Piccolo, M. Rama, A. Zallo

Laboratori Nazionali di Frascati dell'INFN, I-00044 Frascati, Italy

[1]Also with Università di Perugia, Dipartimento di Fisica, Perugia, Italy

3

A. Buzzo, R. Capra, R. Contri, M. Lo Vetere, M. M. Macri, M. R. Monge, S. Passaggio, C. Patrignani,
E. Robutti, A. Santroni, S. Tosi

Università di Genova, Dipartimento di Fisica and INFN, I-16146 Genova, Italy

G. Brandenburg, K. S. Chaisanguanthum, M. Morii, J. Wu

Harvard University, Cambridge, Massachusetts 02138, USA

R. S. Dubitzky, J. Marks, S. Schenk, U. Uwer

Universität Heidelberg, Physikalisches Institut, Philosophenweg 12, D-69120 Heidelberg, Germany

D. J. Bard, W. Bhimji, D. A. Bowerman, P. D. Dauncey, U. Egede, R. L. Flack, J. A. Nash,
M. B. Nikolich, W. Panduro Vazquez

Imperial College London, London, SW7 2AZ, United Kingdom

P. K. Behera, X. Chai, M. J. Charles, U. Mallik, N. T. Meyer, V. Ziegler

University of Iowa, Iowa City, Iowa 52242, USA

J. Cochran, H. B. Crawley, L. Dong, V. Eyges, W. T. Meyer, S. Prell, E. I. Rosenberg, A. E. Rubin

Iowa State University, Ames, Iowa 50011-3160, USA

A. V. Gritsan

Johns Hopkins University, Baltimore, Maryland 21218, USA

A. G. Denig, M. Fritsch, G. Schott

Universität Karlsruhe, Institut für Experimentelle Kernphysik, D-76021 Karlsruhe, Germany

N. Arnaud, M. Davier, G. Grosdidier, A. Höcker, F. Le Diberder, V. Lepeltier, A. M. Lutz, A. Oyanguren,
S. Pruvot, S. Rodier, P. Roudeau, M. H. Schune, A. Stocchi, W. F. Wang, G. Wormser

*Laboratoire de l'Accélérateur Linéaire, IN2P3/CNRS et Université Paris-Sud 11, Centre Scientifique
d'Orsay, B.P. 34, F-91898 ORSAY Cedex, France*

C. H. Cheng, D. J. Lange, D. M. Wright

Lawrence Livermore National Laboratory, Livermore, California 94550, USA

C. A. Chavez, I. J. Forster, J. R. Fry, E. Gabathuler, R. Gamet, K. A. George, D. E. Hutchcroft,
D. J. Payne, K. C. Schofield, C. Touramanis

University of Liverpool, Liverpool L69 7ZE, United Kingdom

A. J. Bevan, F. Di Lodovico, W. Menges, R. Sacco

Queen Mary, University of London, E1 4NS, United Kingdom

G. Cowan, H. U. Flaecher, D. A. Hopkins, P. S. Jackson, T. R. McMahon, S. Ricciardi, F. Salvatore,
A. C. Wren

*University of London, Royal Holloway and Bedford New College, Egham, Surrey TW20 0EX, United
Kingdom*

D. N. Brown, C. L. Davis

University of Louisville, Louisville, Kentucky 40292, USA

J. Allison, N. R. Barlow, R. J. Barlow, Y. M. Chia, C. L. Edgar, G. D. Lafferty, M. T. Naisbit,
J. C. Williams, J. I. Yi

University of Manchester, Manchester M13 9PL, United Kingdom

C. Chen, W. D. Hulsbergen, A. Jawahery, C. K. Lae, D. A. Roberts, G. Simi

University of Maryland, College Park, Maryland 20742, USA

G. Blaylock, C. Dallapiccola, S. S. Hertzbach, X. Li, T. B. Moore, S. Saremi, H. Staengle

University of Massachusetts, Amherst, Massachusetts 01003, USA

R. Cowan, G. Sciolla, S. J. Sekula, M. Spitznagel, F. Taylor, R. K. Yamamoto

Massachusetts Institute of Technology, Laboratory for Nuclear Science, Cambridge, Massachusetts 02139, USA

H. Kim, S. E. Mclachlin, P. M. Patel, S. H. Robertson

McGill University, Montréal, Québec, Canada H3A 2T8

A. Lazzaro, V. Lombardo, F. Palombo

Università di Milano, Dipartimento di Fisica and INFN, I-20133 Milano, Italy

J. M. Bauer, L. Cremaldi, V. Eschenburg, R. Godang, R. Kroeger, D. A. Sanders, D. J. Summers,
H. W. Zhao

University of Mississippi, University, Mississippi 38677, USA

S. Brunet, D. Côté, M. Simard, P. Taras, F. B. Viaud

Université de Montréal, Physique des Particules, Montréal, Québec, Canada H3C 3J7

H. Nicholson

Mount Holyoke College, South Hadley, Massachusetts 01075, USA

N. Cavallo,[2] G. De Nardo, F. Fabozzi,[3] C. Gatto, L. Lista, D. Monorchio, P. Paolucci, D. Piccolo,
C. Sciacca

Università di Napoli Federico II, Dipartimento di Scienze Fisiche and INFN, I-80126, Napoli, Italy

M. A. Baak, G. Raven, H. L. Snoek

NIKHEF, National Institute for Nuclear Physics and High Energy Physics, NL-1009 DB Amsterdam, The Netherlands

C. P. Jessop, J. M. LoSecco

University of Notre Dame, Notre Dame, Indiana 46556, USA

T. Allmendinger, G. Benelli, L. A. Corwin, K. K. Gan, K. Honscheid, D. Hufnagel, P. D. Jackson,
H. Kagan, R. Kass, A. M. Rahimi, J. J. Regensburger, R. Ter-Antonyan, Q. K. Wong

Ohio State University, Columbus, Ohio 43210, USA

N. L. Blount, J. Brau, R. Frey, O. Igonkina, J. A. Kolb, M. Lu, R. Rahmat, N. B. Sinev, D. Strom,
J. Strube, E. Torrence

University of Oregon, Eugene, Oregon 97403, USA

---

[2]Also with Università della Basilicata, Potenza, Italy
[3]Also with Università della Basilicata, Potenza, Italy

A. Gaz, M. Margoni, M. Morandin, A. Pompili, M. Posocco, M. Rotondo, F. Simonetto, R. Stroili, C. Voci

Università di Padova, Dipartimento di Fisica and INFN, I-35131 Padova, Italy

M. Benayoun, H. Briand, J. Chauveau, P. David, L. Del Buono, Ch. de la Vaissière, O. Hamon,
B. L. Hartfiel, M. J. J. John, Ph. Leruste, J. Malclès, J. Ocariz, L. Roos, G. Therin

*Laboratoire de Physique Nucléaire et de Hautes Energies, IN2P3/CNRS, Université Pierre et Marie
Curie-Paris6, Université Denis Diderot-Paris7, F-75252 Paris, France*

L. Gladney, J. Panetta

University of Pennsylvania, Philadelphia, Pennsylvania 19104, USA

M. Biasini, R. Covarelli

Università di Perugia, Dipartimento di Fisica and INFN, I-06100 Perugia, Italy

C. Angelini, G. Batignani, S. Bettarini, F. Bucci, G. Calderini, M. Carpinelli, R. Cenci, F. Forti,
M. A. Giorgi, A. Lusiani, G. Marchiori, M. A. Mazur, M. Morganti, N. Neri, E. Paoloni, G. Rizzo,
J. J. Walsh

Università di Pisa, Dipartimento di Fisica, Scuola Normale Superiore and INFN, I-56127 Pisa, Italy

M. Haire, D. Judd, D. E. Wagoner

Prairie View A&M University, Prairie View, Texas 77446, USA

J. Biesiada, N. Danielson, P. Elmer, Y. P. Lau, C. Lu, J. Olsen, A. J. S. Smith, A. V. Telnov

Princeton University, Princeton, New Jersey 08544, USA

F. Bellini, G. Cavoto, A. D'Orazio, D. del Re, E. Di Marco, R. Faccini, F. Ferrarotto, F. Ferroni,
M. Gaspero, L. Li Gioi, M. A. Mazzoni, S. Morganti, G. Piredda, F. Polci, F. Safai Tehrani, C. Voena

Università di Roma La Sapienza, Dipartimento di Fisica and INFN, I-00185 Roma, Italy

M. Ebert, H. Schröder, R. Waldi

Universität Rostock, D-18051 Rostock, Germany

T. Adye, N. De Groot, B. Franek, E. O. Olaiya, F. F. Wilson

Rutherford Appleton Laboratory, Chilton, Didcot, Oxon, OX11 0QX, United Kingdom

R. Aleksan, S. Emery, A. Gaidot, S. F. Ganzhur, G. Hamel de Monchenault, W. Kozanecki, M. Legendre,
G. Vasseur, Ch. Yèche, M. Zito

DSM/Dapnia, CEA/Saclay, F-91191 Gif-sur-Yvette, France

X. R. Chen, H. Liu, W. Park, M. V. Purohit, J. R. Wilson

University of South Carolina, Columbia, South Carolina 29208, USA

M. T. Allen, D. Aston, R. Bartoldus, P. Bechtle, N. Berger, R. Claus, J. P. Coleman, M. R. Convery,
M. Cristinziani, J. C. Dingfelder, J. Dorfan, G. P. Dubois-Felsmann, D. Dujmic, W. Dunwoodie,
R. C. Field, T. Glanzman, S. J. Gowdy, M. T. Graham, P. Grenier,[4] V. Halyo, C. Hast, T. Hryn'ova,
W. R. Innes, M. H. Kelsey, P. Kim, D. W. G. S. Leith, S. Li, S. Luitz, V. Luth, H. L. Lynch,
D. B. MacFarlane, H. Marsiske, R. Messner, D. R. Muller, C. P. O'Grady, V. E. Ozcan, A. Perazzo,
M. Perl, T. Pulliam, B. N. Ratcliff, A. Roodman, A. A. Salnikov, R. H. Schindler, J. Schwiening,
A. Snyder, J. Stelzer, D. Su, M. K. Sullivan, K. Suzuki, S. K. Swain, J. M. Thompson, J. Va'vra, N. van

---

[4]Also at Laboratoire de Physique Corpusculaire, Clermont-Ferrand, France

Bakel, M. Weaver, A. J. R. Weinstein, W. J. Wisniewski, M. Wittgen, D. H. Wright, A. K. Yarritu, K. Yi, C. C. Young

Stanford Linear Accelerator Center, Stanford, California 94309, USA

P. R. Burchat, A. J. Edwards, S. A. Majewski, B. A. Petersen, C. Roat, L. Wilden

Stanford University, Stanford, California 94305-4060, USA

S. Ahmed, M. S. Alam, R. Bula, J. A. Ernst, V. Jain, B. Pan, M. A. Saeed, F. R. Wappler, S. B. Zain

State University of New York, Albany, New York 12222, USA

W. Bugg, M. Krishnamurthy, S. M. Spanier

University of Tennessee, Knoxville, Tennessee 37996, USA

R. Eckmann, J. L. Ritchie, A. Satpathy, C. J. Schilling, R. F. Schwitters

University of Texas at Austin, Austin, Texas 78712, USA

J. M. Izen, X. C. Lou, S. Ye

University of Texas at Dallas, Richardson, Texas 75083, USA

F. Bianchi, F. Gallo, D. Gamba

Università di Torino, Dipartimento di Fisica Sperimentale and INFN, I-10125 Torino, Italy

M. Bomben, L. Bosisio, C. Cartaro, F. Cossutti, G. Della Ricca, S. Dittongo, L. Lanceri, L. Vitale

Università di Trieste, Dipartimento di Fisica and INFN, I-34127 Trieste, Italy

V. Azzolini, N. Lopez-March, F. Martinez-Vidal

IFIC, Universitat de Valencia-CSIC, E-46071 Valencia, Spain

Sw. Banerjee, B. Bhuyan, C. M. Brown, D. Fortin, K. Hamano, R. Kowalewski, I. M. Nugent, J. M. Roney, R. J. Sobie

University of Victoria, Victoria, British Columbia, Canada V8W 3P6

J. J. Back, P. F. Harrison, T. E. Latham, G. B. Mohanty, M. Pappagallo

Department of Physics, University of Warwick, Coventry CV4 7AL, United Kingdom

H. R. Band, X. Chen, B. Cheng, S. Dasu, M. Datta, K. T. Flood, J. J. Hollar, P. E. Kutter, B. Mellado, A. Mihalyi, Y. Pan, M. Pierini, R. Prepost, S. L. Wu, Z. Yu

University of Wisconsin, Madison, Wisconsin 53706, USA

H. Neal

Yale University, New Haven, Connecticut 06511, USA

1 INTRODUCTION

Measurements of the parameter $\sin2\beta$ [1, 2] have established CP violation in the B^0 meson system and provide strong support for the Kobayashi and Maskawa model of this phenomenon as arising from a single phase in the three-generation CKM quark-mixing matrix [3]. We present, in this paper, results from a time-dependent analysis of the $B^0 \to \pi^+\pi^-\pi^0$ Dalitz plot (DP) that is dominated by the $\rho(770)$ intermediate resonances of all charges and their interference. The goal of the analysis is the simultaneous extraction of the strong transition amplitudes and the weak interaction phase $\alpha \equiv \arg\left[-V_{td}V_{tb}^*/V_{ud}V_{ub}^*\right]$ of the Unitarity Triangle. In the Standard Model, a non-zero value for α is responsible for the occurrence of mixing-induced CP violation in this decay. The *BABAR* and Belle experiments have obtained constraints on α from the measurement of effective quantities $\sin2\alpha_{\mathrm{eff}}$ in B decays to $\pi^+\pi^-$ [4, 5] and from B decays to $\rho^+\rho^-$ [6, 7], using an isospin analysis [8].

Unlike $\pi^+\pi^-$, $\rho^\pm\pi^\mp$ is not a CP eigenstate, and four flavor-charge configurations $(B^0(\overline{B}^0) \to \rho^\pm\pi^\mp)$ must be considered. The corresponding isospin analysis [9] is unfruitful with the present statistics since two pentagonal amplitude relations with 12 unknowns have to be solved (compared to 6 unknowns for the $\pi^+\pi^-$ and $\rho^+\rho^-$ systems). However, it has been pointed out by Snyder and Quinn [10], that one can obtain the necessary degrees of freedom to constrain α without ambiguity by explicitly including in the analysis the variation of the strong phases of the interfering ρ resonances in the Dalitz plot.

1.1 DECAY AMPLITUDES

We consider the decay of a spin-zero B^0 with four-momentum p_B into the three daughters π^+, π^-, π^0, with p_+, p_-, and p_0 their corresponding four-momenta. Using as independent (Mandelstam) variables the invariant squared masses

$$s_+ = (p_+ + p_0)^2 , \qquad s_- = (p_- + p_0)^2 , \tag{1}$$

the invariant squared mass of the positive and negative pion, $s_0 = (p_+ + p_-)^2$, is obtained from energy and momentum conservation

$$s_0 = m_{B^0}^2 + 2m_{\pi^+}^2 + m_{\pi^0}^2 - s_+ - s_- . \tag{2}$$

The differential B^0 decay width with respect to the variables defined in Eq. (1) (*i.e.*, the *Dalitz plot*) reads

$$d\Gamma(B^0 \to \pi^+\pi^-\pi^0) = \frac{1}{(2\pi)^3} \frac{|A_{3\pi}|^2}{8m_{B^0}^3} ds_+ ds_- , \tag{3}$$

where $A_{3\pi}$ is the Lorentz-invariant amplitude of the three-body decay.

We assume in the following that the amplitudes $A_{3\pi}$ and its complex conjugate $\overline{\mathcal{A}}_{3\pi}$, corresponding to the transitions $B^0 \to \pi^+\pi^-\pi^0$ and $\overline{B}^0 \to \pi^+\pi^-\pi^0$, respectively, are dominated by the three resonances ρ^+, ρ^- and ρ^0. The ρ resonances are assumed to be the sum of the ground state $\rho(770)$ and the radial excitations $\rho(1450)$ and $\rho(1700)$, with resonance parameters determined by a combined fit to $\tau^+ \to \overline{\nu}_\tau\pi^+\pi^0$ and $e^+e^- \to \pi^+\pi^-$ data [11]. Since the hadronic environment is different in B decays, we cannot rely on this result and therefore determine the relative $\rho(1450)$ and $\rho(1700)$ amplitudes simultaneously with the CP parameters from the fit. Variations of the other parameters and possible contributions to the $B^0 \to \pi^+\pi^-\pi^0$ decay other than the ρ's are studied as part of the systematic uncertainties (Section 4).

Including the $B^0\overline{B}^0$ mixing parameter q/p into the $\overline{B}^0$ decay amplitudes, we can write [10, 12]

$$A_{3\pi} = f_+A^+ + f_-A^- + f_0A^0 \ , \tag{4}$$

$$\overline{A}_{3\pi} = f_+\overline{A}^+ + f_-\overline{A}^- + f_0\overline{A}^0 \ , \tag{5}$$

where the f_κ (with $\kappa = \{+, -, 0\}$ denote the charge of the ρ from the decay of the B^0 meson) are functions of the Dalitz variables s_+ and s_- that incorporate the kinematic and dynamical properties of the B^0 decay into a (vector) ρ resonance and a (pseudoscalar) pion, and where the A^κ are complex amplitudes that may comprise weak and strong transition phases and that are independent of the Dalitz variables. Note that the definitions (4) and (5) imply the assumption that the relative phases between the $\rho(770)$ and its radial excitations are CP-conserving.

Following Ref. [11], the ρ resonances are parameterized in f_κ by a modified relativistic Breit-Wigner function introduced by Gounaris and Sakurai (GS) [15]. Due to angular momentum conservation, the spin-one ρ resonance is polarized in a helicity-zero state. For a ρ^κ resonance with charge κ, the GS function is multiplied by the kinematic function $-4|\mathbf{p}_\kappa||\mathbf{p}_\tau|\cos\theta_\kappa$, where $\mathbf{p}_\kappa$ is the momentum of either of the daughters of ρ-resonance defined in the ρ-resonance rest frame, and where $\mathbf{p}_\tau$ is the momentum of the particle not from ρ decay defined in the same frame, and $\cos\theta_\kappa$ the cosine of the helicity angle of the ρ^κ. For the ρ^+ (ρ^-), θ_+ (θ_-) is defined by the angle between the π^0 (π^-) in the ρ^+ (ρ^-) rest frame and the ρ^+ (ρ^-) flight direction in the B^0 rest frame. For the ρ^0, θ_0 is defined by the angle between the π^+ in the ρ^0 rest frame and the ρ^0 flight direction in the B^0 rest frame. With these definitions, each pair of GS functions interferes destructively at equal masses-squared.

The occurrence of $\cos\theta_\kappa$ in the kinematic functions substantially enhances the interference between the different ρ bands in the Dalitz plot, and thus increases the sensitivity of this analysis [10].

1.2 TIME DEPENDENCE

With $\Delta t \equiv t_{3\pi} - t_{\mathrm{tag}}$ defined as the proper time interval between the decay of the fully reconstructed $B^0_{3\pi}$ and that of the other meson B^0_{tag}, the time-dependent decay rate $|\mathcal{A}^+_{3\pi}(\Delta t)|^2$ $(|\mathcal{A}^-_{3\pi}(\Delta t)|^2)$ when the tagging meson is a B^0 $(\overline{B}^0)$ is given by

$$|\mathcal{A}^\pm_{3\pi}(\Delta t)|^2 = \frac{e^{-|\Delta t|/\tau_{B^0}}}{4\tau_{B^0}}\left[|A_{3\pi}|^2 + |\overline{A}_{3\pi}|^2 \mp \left(|A_{3\pi}|^2 - |\overline{A}_{3\pi}|^2\right)\cos(\Delta m_d\Delta t) \pm 2\mathrm{Im}\left[\overline{A}_{3\pi}A^*_{3\pi}\right]\sin(\Delta m_d\Delta t)\right] , \tag{6}$$

where τ_{B^0} is the mean B^0 lifetime and Δm_d is the $B^0\overline{B}^0$ oscillation frequency. Here, we have assumed that CP violation in $B^0\overline{B}^0$ mixing is absent $(|q/p| = 1)$, $\Delta\Gamma_{B_d} = 0$ and CPT is conserved. Inserting the amplitudes (4) and (5), one obtains for the terms in Eq. (6)

$$|A_{3\pi}|^2 \pm |\overline{A}_{3\pi}|^2 = \sum_{\kappa\in\{+,-,0\}}|f_\kappa|^2U^\pm_\kappa + 2\sum_{\kappa<\sigma\in\{+,-,0\}}\left(\mathrm{Re}\left[f_\kappa f^*_\sigma\right]U^{\pm,\mathrm{Re}}_{\kappa\sigma} - \mathrm{Im}\left[f_\kappa f^*_\sigma\right]U^{\pm,\mathrm{Im}}_{\kappa\sigma}\right) ,$$

$$\mathrm{Im}\left(\overline{A}_{3\pi}A^*_{3\pi}\right) = \sum_{\kappa\in\{+,-,0\}}|f_\kappa|^2I_\kappa + \sum_{\kappa<\sigma\in\{+,-,0\}}\left(\mathrm{Re}\left[f_\kappa f^*_\sigma\right]I^{\mathrm{Im}}_{\kappa\sigma} + \mathrm{Im}\left[f_\kappa f^*_\sigma\right]I^{\mathrm{Re}}_{\kappa\sigma}\right) , \tag{7}$$

with

$$U_\kappa^\pm = |A^\kappa|^2 \pm |\overline{A}^\kappa|^2 \ , \tag{8}$$

$$U_{\kappa\sigma}^{\pm,\mathrm{Re(Im)}} = \mathrm{Re(Im)} \left[A^\kappa A^{\sigma*} \pm \overline{A}^\kappa \overline{A}^{\sigma*} \right] \ , \tag{9}$$

$$I_\kappa = \mathrm{Im} \left[\overline{A}^\kappa A^{\kappa*} \right] \ , \tag{10}$$

$$I_{\kappa\sigma}^{\mathrm{Re}} = \mathrm{Re} \left[\overline{A}^\kappa A^{\sigma*} - \overline{A}^\sigma A^{\kappa*} \right] \ , \tag{11}$$

$$I_{\kappa\sigma}^{\mathrm{Im}} = \mathrm{Im} \left[\overline{A}^\kappa A^{\sigma*} + \overline{A}^\sigma A^{\kappa*} \right] \ . \tag{12}$$

The 27 coefficients (8)–(12) are real-valued parameters that multiply the $f_\kappa f_\sigma^*$ bilinears (where κ and σ denote the charge of the ρ resonances) [16]. These are the observables that are determined by the fit. Each of the coefficients is related in a unique way to physically more intuitive quantities, such as tree-level and penguin-type amplitudes, the angle α, or the quasi-two-body CP and dilution parameters [17] (*cf.* Section 6). The parameterization (7) is general; the information on the mirror solutions (*e.g.*, on the angle α) that are present in the transition amplitudes A^κ, $\overline{A}^\kappa$ is conserved. In this paper, we determine the relative values of U and I coefficients to U_+^+.

The choice to fit for the U and I coefficients rather than fitting for the complex transition amplitudes and the weak phase α directly is motivated by the following technical simplifications: (*i*) in contrast to the amplitudes, there is a unique solution for the U and I coefficients requiring only a single fit to the selected data sample, (*ii*) in the presence of background, the U and I coefficients are approximately Gaussian distributed, which in general is not the case for the amplitudes, and (*iii*) the propagation of systematic uncertainties and the averaging between different measurements are straightforward for the U's and I's.

The U_κ^+ coefficients are related to resonance fractions (branching fractions and charge asymmetries); the U_κ^- determine the relative abundance of the B^0 decay into $\rho^+\pi^-$ and $\rho^-\pi^+$ and the time-dependent direct CP asymmetries. The I_κ measure mixing-induced CP violation and are sensitive to strong phase shifts. Finally, the $U_{\kappa\sigma}^{\pm,\mathrm{Re(Im)}}$ and $I_{\kappa\sigma}^{\mathrm{Re(Im)}}$ describe the interference pattern in the Dalitz plot, and their presence distinguishes this analysis from the quasi-two-body analysis previously reported in [17]. They represent the additional degrees of freedom that allow one to determine the unknown penguin pollution and the relative strong phases. However, because the overlap regions of the resonances are small and because the events reconstructed in these regions suffer from large misreconstruction rates and background, a substantial data sample is needed to perform a fit that constrains all amplitude parameters.

We determine the quantities of interest in a subsequent least-squares fit to the measured U and I coefficients.

1.3 NORMALIZATION

The decay rate (6) is used as a probability density function (PDF) in a maximum-likelihood fit and must therefore be normalized:

$$|\mathcal{A}_{3\pi}^\pm(\Delta t)|^2 \longrightarrow \frac{1}{\langle |A_{3\pi}|^2 + |\overline{\mathcal{A}}_{3\pi}|^2 \rangle} |\mathcal{A}_{3\pi}^\pm(\Delta t)|^2 \ , \tag{13}$$

where

$$\langle |A_{3\pi}|^2 + |\overline{\mathcal{A}}_{3\pi}|^2 \rangle = \sum_{\kappa \in \{+,-,0\}} \langle |f_\kappa|^2 \rangle U_\kappa^+ \ + \ 2\mathrm{Re} \sum_{\kappa < \sigma \in \{+,-,0\}} \langle f_\kappa f_\sigma^* \rangle \left(U_{\kappa\sigma}^{+,\mathrm{Re}} + i \cdot U_{\kappa\sigma}^{+,\mathrm{Im}} \right) \ . \tag{14}$$

The complex expectation values $\langle f_\kappa f_\sigma^* \rangle$ are obtained from high-statistics Monte Carlo integration of the Dalitz plot (3), taking into account acceptance and resolution effects.

The normalization of the decay rate (6) renders the normalization of the U and I coefficients arbitrary, so that we can fix one coefficient. By convention, we set $U_+^+ \equiv 1$.

1.4 THE SQUARE DALITZ PLOT

Both the signal events and the combinatorial $e^+e^- \to q\bar{q}$ ($q = u, d, s, c$) continuum background events populate the kinematic boundaries of the Dalitz plot due to the low final state masses compared to the B^0 mass. We find the representation (3) is inadequate when one wants to use empirical reference shapes in a maximum-likelihood fit. Large variations occurring in small areas of the Dalitz plot are very difficult to describe in detail. These regions are particularly important since this is where the interference, and hence our ability to determine the strong phases, occurs. We therefore apply the transformation

$$ds_+ \, ds_- \; \longrightarrow |\det J| \, dm' \, d\theta' \; , \tag{15}$$

which defines the *Square Dalitz plot* (SDP). The new coordinates are

$$m' \equiv \frac{1}{\pi} \arccos\left(2\frac{m_0 - m_0^{\min}}{m_0^{\max} - m_0^{\min}} - 1 \right), \; \theta' \equiv \frac{1}{\pi}\theta_0, \tag{16}$$

where m_0 is the invariant mass between the charged tracks, $m_0^{\max} = m_{B^0} - m_{\pi^0}$ and $m_0^{\min} = 2m_{\pi^+}$ are the kinematic limits of m_0, θ_0 is the ρ^0 helicity angle, and J is the Jacobian of the transformation that zooms into the kinematic boundaries of the Dalitz plot. The new variables range between 0 and 1. The determinant of the Jacobian is given by

$$|\det J| \; = \; 4 \, |\mathbf{p}_+^*||\mathbf{p}_0^*| \, m_0 \cdot \frac{\partial m_0}{\partial m'} \cdot \frac{\partial \cos\theta_0}{\partial \theta'} \; , \tag{17}$$

where $|\mathbf{p}_+^*| = \sqrt{E_+^* - m_{\pi^+}^2}$ and $|\mathbf{p}_0^*| = \sqrt{E_0^* - m_{\pi^0}^2}$, and where the energies E_+^* and E_0^* are in the $\pi^+\pi^-$ rest frame. Figure 1 shows the determinant of the Jacobian as a function of the SDP parameters m' and θ'. If the events in the nominal Dalitz plot were distributed according to a uniform (non-resonant) prior, their distribution in the SDP would match the plot of $|\det J|$.

The effect of the transformation (15) can be seen by looking at Figure 2 which displays the nominal and square Dalitz plots for signal events generated with toy Monte Carlo (MC): the homogenization of the distribution is clearly visible. This simulation does not take into account any detector effect and corresponds to a particular choice of the decay amplitudes for which destructive interferences occur at equal ρ masses. To simplify the comparison, hatched areas showing the interference regions between ρ bands and dashed isocontours $\sqrt{s_{+,-,0}} = 1.5$ GeV/c^2 have been superimposed on both Dalitz plots.

2 THE *BABAR* DETECTOR AND DATASET

The data used in this analysis were collected with the *BABAR* detector at the PEP-II asymmetric-energy e^+e^- storage ring at SLAC between October 1999 and June 2006. The sample consists of about 310 fb^{-1}, corresponding to $(346 \pm 3) \times 10^6$ $B\overline{B}$ pairs collected at the $\Upsilon(4S)$ resonance ("on-resonance"), and an integrated luminosity of 21.6 fb^{-1} collected about 40 MeV below the $\Upsilon(4S)$ ("off-resonance").

A detailed description of the *BABAR* detector is presented in Ref. [18]. The tracking system used for track and vertex reconstruction has two main components: a silicon vertex tracker (SVT) and a drift chamber (DCH), both operating within a 1.5 T magnetic field generated by a superconducting solenoidal magnet. Photons are identified in an electromagnetic calorimeter (EMC) surrounding a detector of internally reflected Cherenkov light (DIRC), which associates Cherenkov photons with tracks for particle identification (PID). Muon candidates are identified with the use of the instrumented flux return (IFR) of the solenoid.

3 ANALYSIS METHOD

The U and I coefficients and the $B^0 \to \pi^+\pi^-\pi^0$ event yield are determined by a maximum-likelihood fit of the signal model to the selected candidate events. Kinematic and event shape variables exploiting the characteristic properties of the events are used in the fit to discriminate signal from background.

3.1 EVENT SELECTION AND BACKGROUND SUPPRESSION

We reconstruct $B^0 \to \pi^+\pi^-\pi^0$ candidates from pairs of oppositely-charged tracks, which are required to form a good quality vertex, and a π^0 candidate. In order to ensure that all events are within the Dalitz plot bounaries, we constrain the three-pion invariant mass to the B-mass. We use information from the tracking system, EMC, and DIRC to remove tracks for which the PID is consistent with the electron, kaon, or proton hypotheses. In addition, we require that at least one track has a signature in the IFR that is inconsistent with the muon hypothesis. The π^0 candidate mass must satisfy $0.11 < m(\gamma\gamma) < 0.16\,\mathrm{GeV}/c^2$, where each photon is required to have an energy greater than $50\,\mathrm{MeV}$ in the laboratory frame (LAB) and to exhibit a lateral profile of energy deposition in the EMC consistent with an electromagnetic shower.

A B-meson candidate is characterized kinematically by the energy-substituted mass $m_{\mathrm{ES}} = [(\frac{1}{2}s + \mathbf{p}_0 \cdot \mathbf{p}_B)^2/E_0^2 - \mathbf{p}_B^2]^{\frac{1}{2}}$ and energy difference $\Delta E = E_B^* - \frac{1}{2}\sqrt{s}$, where $(E_B, \mathbf{p}_B)$ and $(E_0, \mathbf{p}_0)$ are the four-vectors of the B-candidate and the initial electron-positron system, respectively. The asterisk denotes the $\Upsilon(4S)$ frame, and s is the square of the invariant mass of the electron-positron system. We require $5.272 < m_{\mathrm{ES}} < 5.288\,\mathrm{GeV}/c^2$, which retains 81% of the signal and 8% of the continuum background events. The ΔE resolution exhibits a dependence on the π^0 energy and therefore varies across the Dalitz plot. We account for this effect by introducing the transformed quantity $\Delta E' = (2\Delta E - \Delta E_+ - \Delta E_-)/(\Delta E_+ - \Delta E_-)$, with $\Delta E_\pm(m_0) = c_\pm - (c_\pm \mp \bar{c})\,(m_0/m_0^{\mathrm{max}})^2$, where m_0 is strongly correlated with the energy of π^0. We use the values $\bar{c} = 0.045\,\mathrm{GeV}$, $c_- = -0.140\,\mathrm{GeV}$, $c_+ = 0.080\,\mathrm{GeV}$, $m_0^{\mathrm{max}} = 5.0\,\mathrm{GeV}$, and require $-1 < \Delta E' < 1$. These values have been obtained from Monte Carlo simulation and are tuned to maximize the selection of correctly reconstructed over misreconstructed signal events. The requirement retains 75% (25%) of the signal (continuum).

Backgrounds arise primarily from random combinations in continuum events. To enhance discrimination between signal and continuum, we use a neural network (NN) [19] to combine four discriminating variables: the angles with respect to the beam axis of the B momentum and B thrust axis in the $\Upsilon(4S)$ frame, and the zeroth and second order monomials $L_{0,2}$ of the energy flow about the B thrust axis. The monomials are defined by $L_j = \sum_i \mathbf{p}_i \times |\cos\theta_i|^j$, where θ_i is the angle with respect to the B thrust axis of track or neutral cluster i, $\mathbf{p}_i$ is its momentum, and the sum excludes the B candidate. The NN is trained in the signal region with off-resonance data and

simulated signal events. The final sample of signal candidates is selected with a requirement on the NN output that retains 77% (8%) of the signal (continuum).

The time difference Δt is obtained from the measured distance between the z positions (along the beam direction) of the $B^0_{3\pi}$ and B^0_{tag} decay vertices, and the boost $\beta\gamma = 0.56$ of the e^+e^- system: $\Delta t = \Delta z/\beta\gamma c$. To determine the flavor of the B^0_{tag} we use the B flavor tagging algorithm of Ref. [22]. This produces six mutually exclusive tagging categories. We also retain untagged events in a seventh category to improve the efficiency of the signal selection and because these events contribute to the measurement of direct CP violation. Events with multiple B candidates passing the full selection occur in 16% ($\rho^\pm\pi^\mp$) and 9% ($\rho^0\pi^0$) of the cases. If the multiple candidates have different π^0's, we choose the candidate with the reconstructed π^0 mass closest to the nominal one; in the case that both candidates have the same π^0, we pick the first one.

The signal efficiency determined from MC simulation is 24% for $B^0 \to \rho^\pm\pi^\mp$ and $B^0 \to \rho^0\pi^0$ events, and 11% for non-resonant $B^0 \to \pi^+\pi^-\pi^0$ events.

Of the selected signal events, 22% of $B^0 \to \rho^\pm\pi^\mp$, 13% of $B^0 \to \rho^0\pi^0$, and 6% of non-resonant events are misreconstructed. Misreconstruced events occur when a track or neutral cluster from the tagging B is assigned to the reconstructed signal candidate. This occurs most often for low-momentum tracks and photons and hence the misreconstructed events concentrate in the corners of the Dalitz plot. Since these are also the areas where the ρ-mesons overlap strongly, it is important to model the misreconstruced events correctly. The details of the model for misreconstructed events over the Dalitz plot is detailed in Section 3.3.1.

3.2 BACKGROUND FROM OTHER B DECAYS

We use MC simulated events to study the background from other B decays. More than a hundred channels have been considered in the preliminary studies, of which twenty-nine have been finally included in the likelihood model – decays with at least two events expected after selection. These exclusive B-background modes are grouped into eighteen different classes gathering decays with similar kinematic and topological properties: six for charged charmless B-decays, eight for neutral charmless B-decays and four for exclusive neutral charmed B-decays. Two additional classes account for inclusive neutral and charged $b \to c$ decays.

Table 1 summarizes the twenty background classes which are used in the fit. For each mode, the expected number of selected events is computed by multiplying the selection efficiency (estimated using MC simulated decays) by the branching fraction scaled up to the dataset luminosity (310 fb^{-1}). The world average branching ratios have been used for the experimentally known decay modes. When only upper limits are given, they have been translated into branching ratios using all information available such as additional conservative hypotheses (e.g. 100% longitudinal polarization for $B \to \rho\rho$ decay) if needed.

3.3 THE MAXIMUM-LIKELIHOOD FIT

We perform an unbinned extended maximum-likelihood fit to extract the inclusive $B^0 \to \pi^+\pi^-\pi^0$ event yield and the U and I coefficients defined in Eqs. (8)–(12). The fit uses the variables m_{ES}, $\Delta E'$, the NN output, and the Dalitz plot to discriminate signal from background. The Δt measurement allows to the determination of mixing-induced CP violation and provides additional continuum-background rejection.

The selected on-resonance data sample is assumed to consist of signal, continuum-background and B-background components, separated by the flavor and tagging category of the tag side B

decay. The signal likelihood consists of the sum of a correctly reconstructed ("truth-matched", TM) component and a misreconstructed ("self-cross-feed", SCF) component.

The probability density function (PDF) $\mathcal{P}_i^c$ for an event i in tagging category c is the sum of the probability densities of all components, namely

$$
\begin{aligned}
\mathcal{P}_i^c \;\equiv\;& N_{3\pi} f_{3\pi}^c \left[(1 - \overline{f}_{\mathrm{SCF}}^c) \mathcal{P}_{3\pi-\mathrm{TM},i}^c + \overline{f}_{\mathrm{SCF}}^c \mathcal{P}_{3\pi-\mathrm{SCF},i}^c \right] \\[8pt]
&+ N_{q\bar{q}}^c \frac{1}{2} \left(1 + q_{\mathrm{tag},i} A_{q\bar{q},\,\mathrm{tag}} \right) \mathcal{P}_{q\bar{q},i}^c \\[8pt]
&+ \sum_{j=1}^{N_{\mathrm{class}}^{B^+}} N_{B^+ j} f_{B^+ j}^c \frac{1}{2} \left(1 + q_{\mathrm{tag},i} A_{B^+,\,\mathrm{tag},j} \right) \mathcal{P}_{B^+,ij}^c \\[8pt]
&+ \sum_{j=1}^{N_{\mathrm{class}}^{B^0}} N_{B^0 j} f_{B^0 j}^c \mathcal{P}_{B^0,ij}^c \;,
\end{aligned}
\tag{18}
$$

where: $N_{3\pi}$ is the total number of $\pi^+\pi^-\pi^0$ signal events in the data sample; $f_{3\pi}^c$ is the fraction of signal events that are tagged in category c; $\overline{f}_{\mathrm{SCF}}^c$ is the fraction of SCF events in tagging category c, averaged over the Dalitz plot; $\mathcal{P}_{3\pi-\mathrm{TM},i}^c$ and $\mathcal{P}_{3\pi-\mathrm{SCF},i}^c$ are the products of PDFs of the discriminating variables used in tagging category c for TM and SCF events, respectively; $N_{q\bar{q}}^c$ is the number of continuum events that are tagged in category c; $q_{\mathrm{tag},i}$ is the tag flavor of the event, defined to be $+1$ for a B_{tag}^0 and -1 for a $\overline{B}_{\mathrm{tag}}^0$; $A_{q\bar{q},\,\mathrm{tag}}$ parameterizes possible tag asymmetry in continuum events; $\mathcal{P}_{q\bar{q},i}^c$ is the continuum PDF for tagging category c; $N_{\mathrm{class}}^{B^+}$ ($N_{\mathrm{class}}^{B^0}$) is the number of charged (neutral) B-related background classes considered in the fit; $N_{B^+ j}$ ($N_{B^0 j}$) is the number of expected events in the charged (neutral) B-background class j; $f_{B^+ j}^c$ ($f_{B^0 j}^c$) is the fraction of charged (neutral) B-background events of class j that are tagged in category c; $A_{B^+,\,\mathrm{tag},j}$ describes a possible tag asymmetry in the charged-B background class j; correlations between the tag and the position in the Dalitz plot (the "charge") are absorbed in tag-flavor-dependent Dalitz plot PDFs that are used for charged-B and continuum background; $\mathcal{P}_{B^+,ij}^c$ is the B^+-background PDF for tagging category c and class j; finally, $\mathcal{P}_{B^0,ij}^c$ is the neutral-B-background PDF for tagging category c and class j.

The PDFs $\mathcal{P}_X^c$ ($X = \{TM, SCF, \mathrm{continuum}, \mathrm{B-bkg}\}$) are the product of the four PDFs of the discriminating variables, $x_1 = m_{ES}$, $x_2 = \Delta E'$, $x_3 = \mathrm{NNoutput}$, and the triplet $x_4 = \{m', \theta', \Delta t\}$:

$$
\mathcal{P}_{X,i(j)}^c \;\equiv\; \prod_{k=1}^{4} P_{X,i(j)}^c(x_k) \;.
\tag{19}
$$

The extended likelihood over all tagging categories is given by

$$
\mathcal{L} \;\equiv\; \prod_{c=1}^{7} e^{-\overline{N}^c} \prod_i^{N^c} \mathcal{P}_i^c \;,
\tag{20}
$$

where $\overline{N}^c$ is the total number of events expected in category c.

A total of 68 parameters, including the inclusive signal yield and the parameters from Eq. (6), are varied in the fit. Most of the parameters describing the continuum distributions are also floated in the fit.

3.3.1 THE Δt AND DALITZ PLOT PDFS

The Dalitz plot PDFs require as input the Dalitz plot-dependent relative selection efficiency, $\epsilon = \epsilon(m', \theta')$, and SCF fraction, $f_{\mathrm{SCF}} = f_{\mathrm{SCF}}(m', \theta')$. Both quantities are taken from MC simulation. Away from the Dalitz plot corners the efficiency is uniform, while it decreases when approaching the corners, where one out of the three bodies in the final state is close to rest so that the acceptance requirements on the particle reconstruction become restrictive. Combinatorial backgrounds and hence SCF fractions are large in the corners of the Dalitz plot due to the presence of soft neutral clusters and tracks.

For an event i, we define the time-dependent Dalitz plot PDFs

$$P_{3\pi-\mathrm{TM},i} \;=\; \varepsilon_i \,(1 - f_{\mathrm{SCF},i}) \,|\det J_i|\,|\mathcal{A}_{3\pi}^{\pm}(\Delta t)|^2 \;, \tag{21}$$

$$P_{3\pi-\mathrm{SCF},\,i} \;=\; \varepsilon_i \, f_{\mathrm{SCF},i} \,|\det J_i|\,|\mathcal{A}_{3\pi}^{\pm}(\Delta t)|^2 \;, \tag{22}$$

where $P_{3\pi-\mathrm{TM},i}$ and $P_{3\pi-\mathrm{SCF},\,i}$ are normalized. The corresponding phase space integration involves the expectation values $\langle \varepsilon\,(1 - f_{\mathrm{SCF}})\,|\det J|\,f^{\kappa}f^{\sigma*}\rangle$ and $\langle \varepsilon\, f_{\mathrm{SCF}}\,|\det J|\,f^{\kappa}f^{\sigma*}\rangle$ for TM and SCF events, where the indices κ, σ run over all resonances belonging to the signal model. The expectation values are model-dependent and are computed with the use of MC integration over the square Dalitz plot:

$$\langle \varepsilon\,(1 - f_{\mathrm{SCF}})\,|\det J|\,f^{\kappa}f^{\sigma*}\rangle \;=\; \frac{\int_0^1 \int_0^1 \varepsilon\,(1 - f_{\mathrm{SCF}})\,|\det J|\,f^{\kappa}f^{\sigma*}\,dm'd\theta'}{\int_0^1 \int_0^1 \varepsilon\,|\det J|\,f^{\kappa}f^{\sigma*}\,dm'd\theta'} \;, \tag{23}$$

and similarly for $\langle \varepsilon\,|\det J|\,f^{\kappa}f^{\sigma*}\rangle$, where all quantities in the integrands are Dalitz plot-dependent.

Equation (18) invokes the phase space-averaged SCF fraction $\overline{f}_{\mathrm{SCF}} \equiv \langle f_{\mathrm{SCF}}\,|\det J|\,f^{\kappa}f^{\sigma*}\rangle$. The PDF normalization is decay-dynamics-dependent and is computed iteratively. We determine the average SCF fractions separately for each tagging category from MC simulation.

The width of the dominant $\rho(770)$ resonance is large compared to the mass resolution for TM events (about $8\,\mathrm{MeV}/c^2$ core Gaussian resolution). We therefore neglect resolution effects in the TM model. Misreconstructed events have a poor mass resolution that strongly varies across the Dalitz plot. It is described in the fit by a 2×2-dimensional resolution function

$$R_{\mathrm{SCF}}(m'_r, \theta'_r, m'_t, \theta'_t) \;, \tag{24}$$

which represents the probability to reconstruct at the coordinate (m'_r, θ'_r) an event that has the true coordinate (m'_t, θ'_t). It obeys the unitarity condition

$$\int_0^1 \int_0^1 R_{\mathrm{SCF}}(m'_r, \theta'_r, m'_t, \theta'_t)\, dm'_r d\theta'_r = 1, \tag{25}$$

and is convolved with the signal model. The R_{SCF} function is obtained from MC simulation.

We use the signal model described in Section 1.1. It contains the dynamical information and is connected with Δt via the matrix element (6), which serves as PDF. It is diluted by the effects of mistagging and the limited vertex resolution [17]. The Δt resolution function for signal and B-background events is a sum of three Gaussian distributions, with parameters determined by a fit to fully reconstructed B^0 decays [22].

The Dalitz plot- and Δt-dependent PDFs factorize for the charged-B-background modes, but not (necessarily) for the neutral-B background due to $B^0\overline{B}^0$ mixing.

15

The charged B-background contribution to the likelihood (18) involves the parameter $A_{B^+, \text{tag}}$, multiplied by the tag flavor q_{tag} of the event. In the presence of significant tag-"charge" correlation (represented by an effective flavor-tag-versus-Dalitz-coordinate correlation), it parameterizes possible direct CP violation in these events. We also use distinct square Dalitz plot PDFs for each reconstructed B flavor tag, and a flavor-tag-averaged PDF for untagged events. The PDFs are obtained from MC simulation and are described with the use of non-parametric functions. The Δt resolution parameters are determined by a fit to fully reconstructed B^+ decays. For each B^+-background class we adjust effective lifetimes to account for the misreconstruction of the event that modifies the nominal Δt resolution function.

The neutral-B background is parameterized with PDFs that depend on the flavor tag of the event. In the case of CP eigenstates, correlations between the flavor tag and the Dalitz coordinate are expected to be small. However, non-CP eigenstates, such as $a_1^{\pm}\pi^{\mp}$, may exhibit such correlation. Both types of decays can have direct and mixing-induced CP violation. A third type of decays involves charged kaons and does not exhibit mixing-induced CP violation, but usually has a strong correlation between the flavor tag and the Dalitz plot coordinate (the kaon charge), because it consists of B-flavor eigenstates. The Dalitz plot PDFs are obtained from MC simulation and are described with the use of non-parametric functions. For neutral B background, the signal Δt resolution model is assumed.

The Dalitz plot treatment of the continuum events is similar to the one used for charged-B background. The square Dalitz plot PDF for continuum background is obtained from on-resonance events selected in the m_{ES} sidebands and corrected for feed-through from B decays. A large number of cross checks has been performed to ensure the high fidelity of the empirical shape parameterization. Analytical models have been found insufficient. The continuum Δt distribution is parameterized as the sum of three Gaussian distributions with common mean and three distinct widths that scale the Δt per-event error. This yields six shape parameters that are determined by the fit. The model is motivated by the observation that the Δt average is independent of its error, and that the Δt RMS depends linearly on the Δt error.

3.3.2 PARAMETERIZATION OF THE OTHER VARIABLES

The m_{ES} distribution of TM signal events is parameterized by a bifurcated Crystal Ball function [21], which is a combination of a one-sided Gaussian and a Crystal Ball function. The mean of this function is determined by the fit. A non-parametric function is used to describe the SCF signal component.

The $\Delta E'$ distribution of TM events is parameterized by a double Gaussian function, where all five parameters depend linearly on m_0^2. Misreconstructed events are parameterized by a broad single Gaussian function.

Both m_{ES} and $\Delta E'$ PDFs are parameterized by non-parametric functions for all B-background classes.

The m_{ES} and $\Delta E'$ PDFs for continuum events are parameterized with an Argus shape function [23] and a second order polynomial, respectively, with parameters determined by the fit.

We use non-parametric functions to empirically describe the distributions of the NN outputs found in the MC simulation for TM and SCF signal events, and for B-background events. We distinguish tagging categories for TM signal events to account for differences observed in the shapes.

The continuum NN distribution is parameterized by a third order polynomial that is defined to be positive. The coefficients of the polynomial are determined by the fit. Continuum events exhibit a correlation between the Dalitz plot coordinate and the shape of the event that is exploited in the

NN. To correct for residual effects, we introduce a linear dependence of the polynomial coefficients on the distance of the Dalitz plot coordinate to the kinematic boundaries of the Dalitz plot. The parameters describing this dependence are determined by the fit.

4   SYSTEMATIC STUDIES

The contributions to the systematic error on the signal parameters are summarized in Table 3. Table 4 summarizes the correlation coefficient extracted from the systematic covariance matrix.

The most important contribution to the systematic uncertainty stems from the signal modeling of the Dalitz plot dynamics.

To estimate the contribution to $B^0 \to \pi^+\pi^-\pi^0$ decay via other resonances and non-resonant decays, we have performed an independent analysis where we include these other decays in the fit model. For simplicity, we assume a uniform Dalitz distribution for the non-resonance events and consider possible resonances including $f_0(980)$, $f_2(1270)$, and a low mass s-wave σ. The fit does not find significant number of any of those decays. However, the inclusion of a low mass $\pi^+\pi^-$ s-wave component degrades our ability to identify $\rho^0\pi^0$ events significantly. The systematic effects (contained in the "Dalitz plot model" field in Table 3) is estimated by observing the difference between the true values and Monte Carlo fit results, in which events are generated based on the new fit results and fit with the nominal setup where only ρ is taken into account.

We vary the mass and width of the $\rho(770)$, $\rho(1450)$ and $\rho(1700)$ within ranges that exceed twice the errors found for these parameters in the fits to τ and e^+e^- data [11], and assign the observed differences in the measured U and I coefficients as systematic uncertainties ("ρ, ρ', ρ'' lineshape" in Table 3). Since some of the U and I coefficients exhibit significant dependence on the $\rho(1450)$ and $\rho(1700)$ contributions, we leave their amplitudes (phases and fractions) free to vary in the nominal fit.

To validate the fitting tool, we perform fits on large MC samples with the measured proportions of signal, continuum and B-background events. No significant biases are observed in these fits. The statistical uncertainties on the fit parameters are taken as systematic uncertainties ("Fit bias" in Table 3).

Another major source of systematic uncertainty is the B-background model. The expected event yields from the background modes are varied according to the uncertainties in the measured or estimated branching fractions ("$N_{\mathrm{Background}}$" in Table 3). Since B-background modes may exhibit CP violation, the corresponding parameters are varied within appropriate uncertainty ranges ("B background CP" in Table 3). As is done for the signal PDFs, we vary the Δt resolution parameters and the flavor-tagging parameters within their uncertainties and assign the differences observed in the on-resonance data fit with respect to nominal fit as systematic errors.

Other systematic effects are much less important to the measurements of U and I coefficients, and they are combined in "Others" field in Table 3. Details are given below.

The parameters for the continuum events are determined by the fit. No additional systematic uncertainties are assigned to them. An exception to this is the Dalitz plot PDF: to estimate the systematic uncertainty from the m_{ES} sideband extrapolation, we select large samples of off-resonance data by loosening the requirements on ΔE and the NN. We compare the distributions of m' and θ' between the m_{ES} sideband and the signal region. No significant differences are found. We assign as systematic error the effect seen when weighting the continuum Dalitz plot PDF by the ratio of both data sets. This effect is mostly statistical in origin.

The uncertainties associated with Δm_d and τ are estimated by varying these parameters within the uncertainties on the world average [20].

The systematic effects due to the signal PDFs comprise uncertainties in the PDF parameterization, the treatment of misreconstructed events, the tagging performance, and the modeling of the signal contributions.

When the signal PDFs are determined from fits to a control sample of fully reconstructed B decays to exclusive final states with charm, the uncertainties are obtained by varying the parameters within the statistical uncertainties. In other cases, the dominant parameters have been left free to vary in the fit, and the differences observed in these fits are taken as systematic errors.

The average fraction of misreconstructed signal events predicted by the MC simulation has been verified with fully reconstructed $B \to D\rho$ events [17]. No significant differences between data and the simulation were found. We vary $\overline{f}_{\text{SCF}}$ for all tagging categories relatively by 25% to estimate the systematic uncertainty.

Tagging efficiencies, dilutions and biases for signal events are varied within their experimental uncertainties.

The systematic errors for the parameters that measure interference effects are dominated by the uncertainty in the signal model, mainly the tail description of the ρ resonance. For the other parameters, the uncertainty on the fit bias and the B-background contamination are important.

5   FIT RESULTS

The maximum-likelihood fit results in the $B^0 \to \pi^+\pi^-\pi^0$ event yield 1847 ± 69, where the error is statistical only. For the U and I coefficients, the results are given together with their statistical and systematic errors in Table 5. The corresponding correlation matrix is given in Table 6. We have generated a sample of Monte Carlo experiments to determine the probability density distributions of the fit parameters. Within the statistical uncertainties of this sample we find Gaussian distributions of the distribution for the fitted U and I coefficients. This allows us to use the least-squares method to derive other quantities from these (Section 6).

The signal is dominated by $B^0 \to \rho^\pm\pi^\mp$ decays. We observe an excess of $\rho^0\pi^0$ events, which is in agreement with our previous upper limit [24], and the latest measurement from the Belle collaboration [25]. The result for the $\rho(1450)$ amplitude is in agreement with the findings in τ and e^+e^- decays [11]. For the relative strong phase between the $\rho(770)$ and the $\rho(1450)$ amplitudes we find $(171 \pm 23)^\circ$ (statistical error only), which is compatible with the result from τ and e^+e^- data.

Figure 3 shows distributions of $\Delta E'$, m_{ES}, the NN output, $\Delta t/\sigma(\Delta t)$, where $\sigma(\Delta t)$ is the per-event error on Δt, as well as the Dalitz plot variables m' and θ', which are enhanced in signal content by requirements on the signal-to-continuum likelihood ratios of the other discriminating variables. Figure 4 shows distribution of the minimum of three di-pion invariant masses, again enhanced in signal content. This plot shows clearly that $\rho(770)$ dominates the signal component.

As a validation of our treatment of the time dependence we allow τ_{B^0} to vary in the fit. We find $\tau_{B^0} = (1.513 \pm 0.066)\,\text{ps}$, while the remaining free parameters are consistent with the nominal fit. To validate the SCF modeling, we leave the average SCF fractions per tagging category free to vary in the fit and find results that are consistent with the MC prediction.

6 INTERPRETATION OF THE RESULTS

The U and I coefficients are related to the quasi-two-body parameters, defined in Ref. [17] as follows

$$C^+ = \frac{U_+^-}{U_+^+} \,, \qquad C^- = \frac{U_-^-}{U_-^+} \,, \qquad S^+ = \frac{2\,I_+}{U_+^+} \,, \qquad S^- = \frac{2\,I_-}{U_-^+} \,, \qquad \mathcal{A}_{\rho\pi} = \frac{U_+^+ - U_-^+}{U_+^+ + U_-^+} \,, \qquad (26)$$

and where $C = (C^+ + C^-)/2$, $\Delta C = (C^+ - C^-)/2$, $S = (S^+ + S^-)/2$, and $\Delta S = (S^+ - S^-)/2$ and $\mathcal{A}_{\rho\pi}$ is the time and flavor integrated asymmetry. In contrast to our previous analysis [17], the definitions of Eq. (26) explicitly account for the presence of interference effects, and are thus exact even for a ρ with finite width, as long as the U and I coefficients are obtained with a Dalitz plot analysis. This treatment leads to a dilution of the result and hence to slightly increased statistical uncertainties compared to neglecting the interference effects.

For the CP-violation parameters, we obtain

$$\mathcal{A}_{\rho\pi} = -0.142 \pm 0.041 \pm 0.015 \,, \qquad (27)$$
$$C = 0.154 \pm 0.090 \pm 0.037 \,, \qquad (28)$$
$$S = 0.01 \pm 0.12 \pm 0.028 \,, \qquad (29)$$

where the first errors given are statistical and the second are the systematic uncertainties. For the other parameters in the quasi-two-body description of the $B^0(\overline{B}^0) \to \rho\pi$ decay-time dependence, we measure

$$\Delta C = 0.377 \pm 0.091 \pm 0.021 \,, \qquad (30)$$
$$\Delta S = 0.06 \pm 0.13 \pm 0.029 \,. \qquad (31)$$

The systematic errors are dominated by the uncertainty on the CP content of the B-related backgrounds. Other contributions are the signal description in the likelihood model (including the limit on non-resonant $B^0 \to \pi^+\pi^-\pi^0$ events), and the fit bias uncertainty. The covariance matrix, including systematic, of the five quasi-two-body parameters is given in Table 7.

One can transform the experimentally convenient, namely uncorrelated, direct CP-violation parameters C and $\mathcal{A}_{\rho\pi}$ into the physically more intuitive quantities $\mathcal{A}_{\rho\pi}^{+-}$, $\mathcal{A}_{\rho\pi}^{-+}$, defined by

$$\mathcal{A}_{\rho\pi}^{+-} = \frac{|\kappa^{+-}|^2 - 1}{|\kappa^{+-}|^2 + 1} = -\frac{\mathcal{A}_{\rho\pi} + C + \mathcal{A}_{\rho\pi}\Delta C}{1 + \Delta C + \mathcal{A}_{\rho\pi}C} \,, \qquad (32)$$

$$\mathcal{A}_{\rho\pi}^{-+} = \frac{|\kappa^{-+}|^2 - 1}{|\kappa^{-+}|^2 + 1} = \frac{\mathcal{A}_{\rho\pi} - C - \mathcal{A}_{\rho\pi}\Delta C}{1 - \Delta C - \mathcal{A}_{\rho\pi}C} \,,$$

where $\kappa^{+-} = (q/p)(\overline{A}^-/A^+)$ and $\kappa^{-+} = (q/p)(\overline{A}^+/A^-)$, so that $\mathcal{A}_{\rho\pi}^{+-}$ ($\mathcal{A}_{\rho\pi}^{-+}$) involves only diagrams where the ρ (π) meson is emitted by the W boson. We find

$$\mathcal{A}_{\rho\pi}^{+-} = 0.03 \pm 0.07 \pm 0.03 \,, \qquad (33)$$
$$\mathcal{A}_{\rho\pi}^{-+} = -0.38\,^{+0.15}_{-0.16} \pm 0.07 \,, \qquad (34)$$

with a correlation coefficient of 0.62 between $\mathcal{A}_{\rho\pi}^{+-}$ and $\mathcal{A}_{\rho\pi}^{-+}$. The confidence level contours including systematic errors are given in Fig. 5. The significance, including systematic uncertainties and

calculated by using a mininum χ^2 method, for the observation of non-zero direct CP violation is at the 3.0σ level. The evidence of direct CP violation is almost entirely from the $B^0 \to \rho^-\pi^+$ decays.

The measurement of the resonance interference terms allows us to determine the relative phase

$$\delta_{+-} = \arg\left(A^{+*}A^-\right) , \tag{35}$$

between the amplitudes of the decays $B^0 \to \rho^-\pi^+$ and $B^0 \to \rho^+\pi^-$. Through the definitions (8)–(12), we can derive a constraint on δ_{+-} from the measured U and I coefficients by performing a least-squares minimization with the six complex amplitudes as free parameters. The constraint can be improved with the use of strong isospin symmetry. The amplitudes A^κ represent the sum of tree-level and penguin-type amplitudes, which have different CKM factors: the tree-level (T^κ) $B^0 \to \rho^\kappa\pi^{\overline{\kappa}}$ transition amplitude is proportional to $V_{ud}V_{ub}^*$, while the corresponding penguin-type amplitude (P^κ) comes with $V_{qd}V_{qb}^*$, where $q = u, c, t$. Here we denote by $\overline{\kappa}$ the charge conjugate of κ, where $\overline{0} = 0$. Using the unitarity of the CKM matrix one can reorganize the amplitudes and obtain [12]

$$\begin{aligned}
A^\kappa &= T^\kappa e^{-i\alpha} + P^\kappa , \\
\overline{A}^\kappa &= T^{\overline{\kappa}} e^{+i\alpha} + P^{\overline{\kappa}} ,
\end{aligned} \tag{36}$$

where the magnitudes of the CKM factors have been absorbed in the T^κ, P^κ, $T^{\overline{\kappa}}$ and $P^{\overline{\kappa}}$. The Eqs. (36) represent 13 unknowns of which two can be fixed due to an arbitrary global phase and the normalization condition $U_+^+ = 1$. Using strong isospin symmetry and neglecting isospin-breaking effects, one can identify $P^0 = -(P^+ + P^-)/2$, which reduces the number of unknowns to be determined by the fit to 9. This set of parameters provides the constraint on δ_{+-}, shown in the left plot of Fig. 6. We find for the solution that is favored by the fit

$$\delta_{+-} = (34 \pm 29)^\circ , \tag{37}$$

where the errors include both statistical and systematic effects. There is a clear structure of multiple solutions which give comparable χ^2. Only a marginal constraint on δ_{+-} is obtained for C.L. < 0.05.

Finally, following the same procedure, we can also derive a constraint on α from the measured U and I coefficients. The resulting C.L. function versus α is given in the right hand plot of Fig. 6. It includes systematic uncertainties. Ignoring the mirror solution at $\alpha + 180^\circ$, we find $\alpha \in (75^\circ, 152^\circ)$ at 68% C.L. No constraint on α is achieved at two sigma and beyond.

7 SUMMARY

We have presented the preliminary measurement of CP-violating asymmetries in $B^0 \to \pi^+\pi^-\pi^0$ decays dominated by the ρ resonance. The results are obtained from a data sample of 347 million $\Upsilon(4S) \to B\overline{B}$ decays. We perform a time-dependent Dalitz plot analysis. From the measurement of the coefficients of 26 form factor bilinears we determine the three CP-violating and two CP-conserving quasi-two-body parameters, where we find a 3.0σ evidence of direct CP violation. Taking advantage of the interference between the ρ resonances in the Dalitz plot, we derive constraints on the relative strong phase between B^0 decays to $\rho^+\pi^-$ and $\rho^-\pi^+$, and on the angle α of the Unitarity Triangle. These measurements are consistent with the expectation from the CKM fit [26].

8   Acknowledgments

References

[1] *BABAR* Collaboration (B. Aubert *et al.*), Phys. Rev. Lett. **89**, 201802 (2002).

[2] Belle Collaboration (K. Abe *et al.*), Phys. Rev. D **66**, 071102 (2002).

[3] N. Cabibbo, Phys. Rev. Lett. **10**, 531 (1963); M. Kobayashi and T. Maskawa, Prog. Theor. Phys. **49**, 652 (1973).

[4] *BABAR* Collaboration, B. Aubert *et al.*, Phys. Rev. Lett. **89**, 281802 (2002); A. Jawahery, Int. J. Mod. Phys. A **19**, 975 (2004)

[5] Belle Collaboration (K. Abe *et al.*), *Phys. Rev. Lett.* **93**, 021601 (2004).

[6] *BABAR* Collaboration (B. Aubert *et al.*), *Phys. Rev. Lett.* **93**, 231801 (2004).

[7] Belle Collaboration (K. Abe *et al.*), *Phys. Rev. Lett.* **96**, 171801 (2006).

[8] M. Gronau and D. London, *Phys. Rev. Lett.* **65**, 3381 (1990).

[9] H.J. Lipkin, Y. Nir, H.R. Quinn and A. Snyder, Phys. Rev. **D44**, 1454 (1991).

[10] H.R. Quinn and A.E. Snyder, Phys. Rev. **D48**, 2139 (1993).

[11] ALEPH Collaboration, (R. Barate *et al.*), Z. Phys. **C76**, 15 (1997); we use updated lineshape fits including new data from e^+e^- annihilation [13] and τ spectral functions [14] (masses and widths in MeV/c^2): $m_{\rho^\pm(770)} = 775.5 \pm 0.6$, $m_{\rho^0(770)} = 773.1 \pm 0.5$, $\Gamma_{\rho^\pm(770)} = 148.2 \pm 0.8$, $\Gamma_{\rho^\pm(770)} = 148.0 \pm 0.9$, $m_{\rho(1450)} = 1409 \pm 12$, $\Gamma_{\rho(1450)} = 500 \pm 37$, $m_{\rho(1700)} = 1749 \pm 20$, and $\Gamma_{\rho(1700)} \equiv 235$.

[12] The *BABAR* Physics Book, Editors P.F. Harrison and H.R. Quinn, SLAC-R-504 (1998).

[13] R.R. Akhmetshin *et al.* (CMD-2 Collaboration), *Phys. Lett.* **B527**, 161 (2002).

[14] ALEPH Collaboration, ALEPH 2002-030 CONF 2002-019, (July 2002).

[15] G.J. Gounaris and J.J. Sakurai, Phys. Rev. Lett. **21**, 244 (1968).

[16] H.R. Quinn and J. Silva, Phys. Rev. **D62**, 054002 (2000).

[17] *BABAR* Collaboration (B. Aubert *et al.*), Phys. Rev. Lett. **91**, 201802 (2003); updated preliminary results at *BABAR*-PLOT-0055 (2003).

[18] *BABAR* Collaboration, B. Aubert *et al.*, Nucl. Instrum. Methods **A479**, 1 (2002).

[19] P. Gay, B. Michel, J. Proriol, and O. Deschamps, *"Tagging Higgs Bosons in Hadronic LEP-2 Events with Neural Networks."*, In Pisa 1995, New computing techniques in physics research, 725 (1995).

[20] Particle Data Group (S. Eidelman *et al.*), Phys. Lett. **B592**, 1 (2004).

[21] T. Skwarnicki, DESY F31-86-02, Ph.D. thesis (1986); see also Ref. [22].

[22] *BABAR* Collaboration, B. Aubert *et al.*, Phys. Rev. **D66**, 032003 (2002).

[23] ARGUS Collaboration (H. Albrecht *et al.*), Z. Phys. C **48**, 543 (1990; see also Ref. [22]).

[24] *BABAR* Collaboration (B. Aubert *et al.*), Phys. Rev. Lett. **93**, 051802 (2004).

[25] Belle Collaboration (J. Dragic *et al.*), Phys. Rev. **D73**, 111105 (2006).

[26] J. Charles *et al.*, Eur. Phys. J. **C41**, 1 (2005).
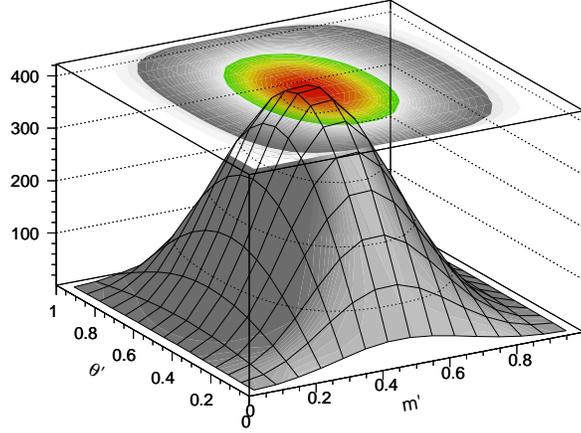
Figure 1: Jacobian determinant (17) of the transformation (15) defining the SDP. Such pattern would be obtained in the SDP if events were uniformly distributed over the nominal Dalitz plot.
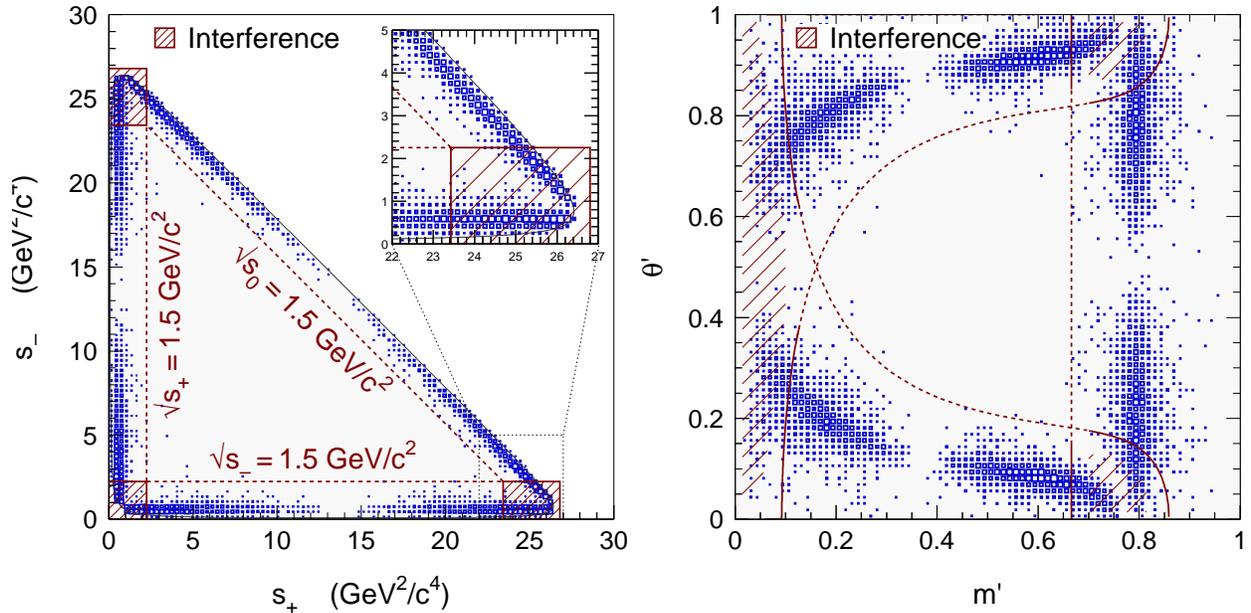
Figure 2: Nominal (left) and square (right) Dalitz plots for Monte-Carlo generated $B^0 \to \pi^+\pi^-\pi^0$ decays. Comparing the two Dalitz plots shows that the transformation (15) indeed homogenizes the distribution of events which are no more along the plot boundaries but rather cover a larger fraction of the physical region. The decays have been simulated without any detector effect and the amplitudes A^+, A^- and A^0 have all been chosen equal to 1 in order to have destructive interferences at equal ρ masses. The main overlap regions between the charged and neutral ρ bands are indicated by the hatched areas. Dashed lines in both plots correspond to $\sqrt{s_{+,-,0}} = 1.5$ GeV/c^2: the central region of the Dalitz plot (defined by requiring that all 3 two-body invariant masses exceed this threshold) contains almost no signal event.

Class	Mode	BR [10^{-6}]	Expected number of events
0	$B^+ \to \rho^+ \rho^0_{[\text{long}]}$	19.1 ± 3.5	52 ± 10
0	$B^+ \to a_1^+(\to (\rho\pi)^+)\pi^0$	20.0 ± 15.0	32 ± 24
0	$B^+ \to a_1^0(\to \rho^{+-}\pi^{-+})\pi^+$	20.0 ± 15.0	19 ± 14
1	$B^+ \to \pi^+ \rho^0$	8.7 ± 1.0	73 ± 8
1	$B^+ \to \rho^0 K^+$	4.3 ± 0.6	6 ± 1
2	$B^+ \to \pi^+ K_S^0(\to \pi^+\pi^-)$	8.3 ± 0.4	10 ± 1
3	$B^+ \to \pi^0 \rho^+$	10.8 ± 1.4	63 ± 8
3	$B^+ \to \pi^+ K_S^0(\to \pi^0\pi^0)$	3.7 ± 0.2	15 ± 2
4	$B^+ \to \pi^+ \pi^0$	5.5 ± 0.6	14 ± 2
4	$B^+ \to K^+ \pi^0$	12.1 ± 0.8	8 ± 1
5	$B^+ \to (K^{(**)}(1430)\pi)^+ \to (K^+\pi\pi)^+$	29.0 ± 5.4	38 ± 5
6	$B^0 \to \pi^- K^{\star+}(\to K_S^0\pi^+)$	3.3 ± 0.4	2 ± 1
7	$B^0 \to \rho^+ \rho^-_{[\text{long}]}$	25.2 ± 3.7	67 ± 10
7	$B^0 \to (a_1\pi)^0$	39.7 ± 3.7	39 ± 4
8	$B^0 \to K^+ \pi^-$	18.9 ± 0.7	12 ± 0
9	$B^0 \to \pi^- K^{\star+}(\to K^+\pi^0)$	3.3 ± 0.4	20 ± 2
9	$B^0 \to K^{(**)}(1430)\pi \to K\pi\pi^0$	11.2 ± 2.2	212 ± 34
10	$B^0 \to \gamma K^{\star 0}(892, 1430)(\to (K^+\pi^-)^0)$	27.4 ± 1.5	14 ± 1
10	$B^0 \to \pi^0 K^{\star 0}(\to K^+\pi^-)$	1.3 ± 0.5	9 ± 4
10	$B^0 \to \eta'(\to \rho^0\gamma)\pi^0$	0.4 ± 0.2	3 ± 2
11	$B^0 \to \rho^- K^+$	9.9 ± 1.6	103 ± 17
12	$B^0 \to K^+ \pi^- \pi^0_{[\text{nonres}]}$	4.6 ± 4.6	38 ± 38
13	$B^0 \to \pi^0 K_S^0(\to \pi^+\pi^-)$	5.8 ± 0.5	50 ± 4
14	$B^0 \to D^-(\to \pi^-\pi^0)\pi^+$	7.5 ± 2.3	599 ± 184
15	$B^0 \to \overline{D}^0(\to K^+\pi^-)\pi^0$	11.0 ± 3.2	100 ± 29
16	$B^0 \to \overline{D}^0(\to \pi^+\pi^-)\pi^0$	0.4 ± 0.1	35 ± 9
17	$B^0 \to J/\psi(\to e^+e^-, \mu^+\mu^-)\pi^0$	2.6 ± 0.5	77 ± 15
18	$B^0 \to \{\text{neutral generic } b \to c \text{ decays}\}$	$-$	173 ± 15
19	$B^+ \to \{\text{charged generic } b \to c \text{ decays}\}$	$-$	396 ± 20

Table 1: Summary of the B-background modes taken into account for the likelihood model. They have been grouped in twenty classes: charged charmless (six), neutral charmless (eight), exclusive neutral charmed (four) and inclusive neutral and charged charmed decays. Modes with at least two events expected after final selection have been included.

Variable	TM Signal	SCF Signal	Continuum	B-Background
ΔE	GG	G	P2	NP
m_{ES}	biCB	NP	Argus	NP
Neural Net	NP	NP	P3	NP
Dalitz	see text	see text	NP	NP
Δt	GGG	GGG	GGG	GGG

Table 2: Summary of PDF parameterizations where G=Gaussian, PX=X-order polynomial, NP=non-parametric, and biCB=bifurcated Crystal Ball. See Section 3.3.1 for a detailed description of the Dalitz plot parameterization for signal.

	I_0	I_-	I_{-0}^{Im}	I_{-0}^{Re}	I_+	I_{+0}^{Im}
Dalitz plot model	0.010	0.006	0.110	0.102	0.020	0.018
ρ,ρ',ρ'' lineshape	0.003	0.012	0.240	0.103	0.009	0.225
Fit bias	0.014	0.023	0.173	0.375	0.008	0.186
$N_{\mathrm{Background}}$	0.002	0.008	0.064	0.085	0.005	0.026
B background CP	0.005	0.009	0.082	0.061	0.011	0.039
Others	0.002	0.006	0.104	0.052	0.005	0.051
Sum	0.017	0.027	0.315	0.402	0.023	0.292

	I_{+0}^{Re}	I_{+-}^{Im}	I_{+-}^{Re}	U_0^-	U_0^+	$U_{-0}^{-,\mathrm{Im}}$	$U_{-0}^{-,\mathrm{Re}}$
Dalitz plot model	0.017	0.007	0.127	0.082	0.041	0.144	0.209
ρ,ρ',ρ'' lineshape	0.308	0.138	0.306	0.012	0.012	0.086	0.159
Fit bias	0.301	0.036	0.048	0.088	0.001	0.050	0.087
$N_{\mathrm{Background}}$	0.049	0.178	0.176	0.002	0.009	0.034	0.045
B background CP	0.042	0.044	0.095	0.015	0.002	0.020	0.073
Others	0.073	0.059	0.095	0.004	0.002	0.012	0.050
Sum	0.431	0.143	0.335	0.121	0.043	0.175	0.276

	$U_{-0}^{+,\mathrm{Im}}$	$U_{-0}^{+,\mathrm{Re}}$	U_-^-	U_-^+	$U_{+0}^{-,\mathrm{Im}}$	$U_{+0}^{-,\mathrm{Re}}$	$U_{+0}^{+,\mathrm{Im}}$
Dalitz plot model	0.034	0.024	0.022	0.030	0.036	0.258	0.076
ρ,ρ',ρ'' lineshape	0.222	0.045	0.010	0.030	0.050	0.216	0.089
Fit bias	0.034	0.058	0.004	0.005	0.053	0.007	0.004
$N_{\mathrm{Background}}$	0.045	0.017	0.013	0.005	0.117	0.103	0.034
B background CP	0.032	0.018	0.032	0.009	0.063	0.075	0.019
Others	0.027	0.015	0.010	0.002	0.045	0.020	0.027
Sum	0.227	0.078	0.025	0.043	0.082	0.337	0.117

	$U_{+0}^{+,\mathrm{Re}}$	$U_{+-}^{-,\mathrm{Im}}$	$U_{+-}^{-,\mathrm{Re}}$	$U_{+-}^{+,\mathrm{Im}}$	$U_{+-}^{+,\mathrm{Re}}$	U_+^-
Dalitz plot model	0.045	0.014	0.250	0.703	0.227	0.010
ρ,ρ',ρ'' lineshape	0.140	0.169	0.200	0.169	0.159	0.031
Fit bias	0.020	0.007	0.069	0.012	0.033	0.027
$N_{\mathrm{Background}}$	0.069	0.137	0.122	0.024	0.166	0.014
B background CP	0.014	0.042	0.029	0.025	0.025	0.034
Others	0.024	0.032	0.067	0.024	0.044	0.009
Sum	0.148	0.170	0.328	0.723	0.279	0.042

	$\mathcal{A}_{\rho\pi}$	C	ΔC	S	ΔS
Dalitz plot model	0.008	0.002	0.013	0.015	0.024
ρ,ρ',ρ'' lineshape	0.011	0.021	0.011	0.016	0.008
Fit bias	0.004	0.012	0.015	0.028	0.011
$N_{\mathrm{Background}}$	0.002	0.005	0.011	0.002	0.011
B background CP	0.003	0.029	0.006	0.017	0.005
Others	0.001	0.007	0.005	0.006	0.007
Sum	0.015	0.037	0.021	0.028	0.029

Table 3: Summary of systematic uncertainties.

	$N_{3\pi}$	I_0	I_-	I_{-0}^{Im}	I_{-0}^{Re}	I_+	I_{+0}^{Im}	I_{+0}^{Re}	I_{+-}^{Im}	I_{+-}^{Re}	U_0^-	U_0^+	$U_{-0}^{-,Im}$
$N_{3\pi}$	1.00												
I_0	0.29	1.00											
I_-	0.12	−0.68	1.00										
I_{-0}^{Im}	−0.18	−0.61	0.73	1.00									
I_{-0}^{Re}	−0.07	0.84	−0.82	−0.60	1.00								
I_+	0.72	0.18	0.24	−0.03	−0.05	1.00							
I_{+0}^{Im}	0.10	−0.57	0.73	0.75	−0.61	0.40	1.00						
I_{+0}^{Re}	−0.28	0.59	−0.66	−0.43	0.62	−0.48	−0.79	1.00					
I_{+-}^{Im}	0.18	0.13	0.14	0.01	−0.08	0.03	0.23	−0.21	1.00				
I_{+-}^{Re}	0.35	0.12	0.08	0.13	−0.17	−0.09	−0.14	0.38	−0.01	1.00			
U_0^-	0.79	−0.15	0.41	0.13	−0.49	0.70	0.38	−0.46	−0.10	0.36	1.00		
U_0^+	−0.83	−0.53	0.27	0.46	−0.22	−0.69	0.16	0.01	−0.00	−0.22	−0.66	1.00	
$U_{-0}^{-,Im}$	−0.83	−0.28	0.01	0.26	0.07	−0.47	0.17	−0.08	0.13	−0.65	−0.77	0.79	1.00
$U_{-0}^{-,Re}$	0.70	0.23	−0.05	−0.33	−0.13	0.51	−0.07	0.05	0.01	0.51	0.72	−0.76	−0.83
$U_{-0}^{+,Im}$	−0.22	0.21	−0.41	−0.57	0.10	−0.29	−0.52	0.47	−0.00	0.03	−0.12	−0.09	−0.05
$U_{-0}^{+,Re}$	−0.39	0.32	−0.43	−0.27	0.55	−0.31	−0.24	0.14	0.31	−0.51	−0.76	0.27	0.60
U_-^-	−0.36	−0.25	0.12	0.05	−0.22	−0.39	−0.06	0.04	0.05	−0.08	−0.22	0.40	0.30
U_-^+	0.48	0.57	−0.40	−0.45	0.24	0.36	−0.32	0.42	−0.05	0.47	0.44	−0.73	−0.68
$U_{+0}^{-,Im}$	0.30	0.42	−0.24	−0.51	0.28	0.04	−0.25	0.11	0.55	−0.03	−0.09	−0.27	−0.15
$U_{+0}^{-,Re}$	−0.61	−0.29	−0.01	−0.08	−0.24	−0.76	−0.34	0.38	0.03	0.12	−0.45	0.57	0.31
$U_{+0}^{+,Im}$	−0.57	−0.37	0.04	0.01	−0.06	−0.18	0.22	−0.37	0.01	−0.84	−0.40	0.47	0.77
$U_{+0}^{+,Re}$	0.40	0.15	0.10	−0.02	0.15	0.34	0.25	−0.50	0.45	−0.35	0.02	−0.18	0.04
$U_{+-}^{-,Im}$	−0.17	−0.20	0.22	0.61	0.02	0.20	0.57	−0.35	−0.15	−0.28	−0.07	0.22	0.40
$U_{+-}^{-,Re}$	0.45	0.53	−0.25	−0.01	0.36	0.45	−0.03	0.33	−0.20	0.48	0.35	−0.56	−0.53
$U_{+-}^{+,Im}$	−0.89	−0.54	0.19	0.31	−0.28	−0.68	0.12	−0.04	0.06	−0.38	−0.64	0.88	0.84
$U_{+-}^{+,Re}$	0.56	0.20	0.00	0.13	0.18	0.70	0.28	−0.30	−0.29	0.00	0.50	−0.55	−0.37
U_+^-	−0.04	0.56	−0.54	−0.44	0.44	−0.16	−0.53	0.65	−0.02	0.30	−0.13	−0.23	−0.18

	$U_{-0}^{-,Re}$	$U_{-0}^{+,Im}$	$U_{-0}^{+,Re}$	U_-^-	U_-^+	$U_{+0}^{-,Im}$	$U_{+0}^{-,Re}$	$U_{+0}^{+,Im}$	$U_{+0}^{+,Re}$	$U_{+-}^{-,Im}$	$U_{+-}^{-,Re}$	$U_{+-}^{+,Im}$	$U_{+-}^{+,Re}$	U_+^-
$U_{-0}^{-,Re}$	1.00													
$U_{-0}^{+,Im}$	0.33	1.00												
$U_{-0}^{+,Re}$	−0.54	−0.07	1.00											
U_-^-	−0.34	0.22	0.02	1.00										
U_-^+	0.80	0.50	−0.41	−0.31	1.00									
$U_{+0}^{-,Im}$	0.22	0.21	0.32	0.10	0.18	1.00								
$U_{+0}^{-,Re}$	−0.15	0.60	0.07	0.49	−0.15	0.11	1.00							
$U_{+0}^{+,Im}$	−0.55	0.17	0.40	0.27	−0.52	−0.10	0.17	1.00						
$U_{+0}^{+,Re}$	−0.20	−0.59	0.48	−0.16	−0.37	0.42	−0.54	0.10	1.00					
$U_{+-}^{-,Im}$	−0.48	−0.70	0.10	−0.19	−0.39	−0.53	−0.56	0.21	0.23	1.00				
$U_{+-}^{-,Re}$	0.48	−0.20	−0.30	−0.51	0.65	−0.08	−0.55	−0.69	−0.13	0.21	1.00			
$U_{+-}^{+,Im}$	−0.68	0.21	0.30	0.48	−0.62	−0.24	0.68	0.68	−0.28	0.09	−0.72	1.00		
$U_{+-}^{+,Re}$	0.20	−0.62	−0.19	−0.47	0.18	−0.27	−0.91	−0.28	0.35	0.60	0.61	−0.68	1.00	
U_+^-	0.20	0.48	−0.02	0.34	0.56	0.30	0.19	−0.29	−0.36	−0.33	0.31	−0.17	−0.14	1.00

Table 4: Correlation matrix of systematic uncertainties for the U and I coefficients. Note that all elements above the diagonal are omitted for readability.

Parameter	Description	Result
U_0^+	Coefficient of $|f_0|^2$	$0.237 \pm 0.053 \pm 0.043$
U_-^+	Coefficient of $|f_-|^2$	$1.33 \pm 0.11 \pm 0.04$
U_0^-	Coefficient of $|f_0|^2 \cos(\Delta m_d \Delta t)$	$-0.055 \pm 0.098 \pm 0.13$
U_-^-	Coefficient of $|f_-|^2 \cos(\Delta m_d \Delta t)$	$-0.30 \pm 0.15 \pm 0.03$
U_+^-	Coefficient of $|f_+|^2 \cos(\Delta m_d \Delta t)$	$0.53 \pm 0.15 \pm 0.04$
I_0	Coefficient of $|f_0|^2 \sin(\Delta m_d \Delta t)$	$-0.028 \pm 0.058 \pm 0.02$
I_-	Coefficient of $|f_-|^2 \sin(\Delta m_d \Delta t)$	$-0.03 \pm 0.10 \pm 0.03$
I_+	Coefficient of $|f_+|^2 \sin(\Delta m_d \Delta t)$	$0.039 \pm 0.097 \pm 0.02$
$U_{+-}^{+,\mathrm{Im}}$	Coefficient of $\mathrm{Im}[f_+ f_-^*]$	$0.62 \pm 0.54 \pm 0.72$
$U_{+-}^{+,\mathrm{Re}}$	Coefficient of $\mathrm{Re}[f_+ f_-^*]$	$0.38 \pm 0.55 \pm 0.28$
$U_{+-}^{-,\mathrm{Im}}$	Coefficient of $\mathrm{Im}[f_+ f_-^*] \cos(\Delta m_d \Delta t)$	$0.13 \pm 0.94 \pm 0.17$
$U_{+-}^{-,\mathrm{Re}}$	Coefficient of $\mathrm{Re}[f_+ f_-^*] \cos(\Delta m_d \Delta t)$	$2.14 \pm 0.91 \pm 0.33$
I_{+-}^{Im}	Coefficient of $\mathrm{Im}[f_+ f_-^*] \sin(\Delta m_d \Delta t)$	$-1.9 \pm 1.1 \pm 0.1$
I_{+-}^{Re}	Coefficient of $\mathrm{Re}[f_+ f_-^*] \sin(\Delta m_d \Delta t)$	$-0.1 \pm 1.9 \pm 0.3$
$U_{+0}^{+,\mathrm{Im}}$	Coefficient of $\mathrm{Im}[f_+ f_0^*]$	$0.03 \pm 0.42 \pm 0.12$
$U_{+0}^{+,\mathrm{Re}}$	Coefficient of $\mathrm{Re}[f_+ f_0^*]$	$-0.75 \pm 0.40 \pm 0.15$
$U_{+0}^{-,\mathrm{Im}}$	Coefficient of $\mathrm{Im}[f_+ f_0^*] \cos(\Delta m_d \Delta t)$	$-0.93 \pm 0.68 \pm 0.08$
$U_{+0}^{-,\mathrm{Re}}$	Coefficient of $\mathrm{Re}[f_+ f_0^*] \cos(\Delta m_d \Delta t)$	$-0.47 \pm 0.80 \pm 0.3$
I_{+0}^{Im}	Coefficient of $\mathrm{Im}[f_+ f_0^*] \sin(\Delta m_d \Delta t)$	$-0.1 \pm 1.1 \pm 0.3$
I_{+0}^{Re}	Coefficient of $\mathrm{Re}[f_+ f_0^*] \sin(\Delta m_d \Delta t)$	$0.2 \pm 1.1 \pm 0.4$
$U_{-0}^{+,\mathrm{Im}}$	Coefficient of $\mathrm{Im}[f_- f_0^*]$	$-0.03 \pm 0.40 \pm 0.23$
$U_{-0}^{+,\mathrm{Re}}$	Coefficient of $\mathrm{Re}[f_- f_0^*]$	$-0.52 \pm 0.32 \pm 0.08$
$U_{-0}^{-,\mathrm{Im}}$	Coefficient of $\mathrm{Im}[f_- f_0^*] \cos(\Delta m_d \Delta t)$	$0.24 \pm 0.61 \pm 0.2$
$U_{-0}^{-,\mathrm{Re}}$	Coefficient of $\mathrm{Re}[f_- f_0^*] \cos(\Delta m_d \Delta t)$	$-0.42 \pm 0.73 \pm 0.28$
I_{-0}^{Im}	Coefficient of $\mathrm{Im}[f_- f_0^*] \sin(\Delta m_d \Delta t)$	$0.7 \pm 1.0 \pm 0.3$
I_{-0}^{Re}	Coefficient of $\mathrm{Re}[f_- f_0^*] \sin(\Delta m_d \Delta t)$	$0.92 \pm 0.91 \pm 0.4$

Table 5: Fit results for the U and I coefficients. The errors given are statistical (first) and systematic (second). The free normalization parameter U_+^+ is fixed to 1.

	$N_{3\pi}$	I_0	I_-	I_{-0}^{Im}	I_{-0}^{Re}	I_+	I_{+0}^{Im}	I_{+0}^{Re}	I_{+-}^{Im}	I_{+-}^{Re}	U_0^-	U_0^+	$U_{-0}^{-,\mathrm{Im}}$
$N_{3\pi}$	1.00												
I_0	0.02	1.00											
I_-	0.04	−0.07	1.00										
I_{-0}^{Im}	0.00	−0.06	0.20	1.00									
I_{-0}^{Re}	−0.06	0.16	−0.17	−0.12	1.00								
I_+	−0.02	−0.01	−0.08	−0.13	0.12	1.00							
I_{+0}^{Im}	0.01	0.03	−0.03	−0.05	0.02	0.27	1.00						
I_{+0}^{Re}	−0.01	0.08	0.03	0.11	−0.04	−0.20	−0.36	1.00					
I_{+-}^{Im}	0.07	0.01	0.10	−0.05	0.01	0.29	0.10	−0.07	1.00				
I_{+-}^{Re}	0.04	−0.01	0.16	0.28	−0.23	−0.32	−0.11	0.21	−0.06	1.00			
U_0^-	0.04	0.05	−0.00	−0.12	−0.25	−0.01	0.03	−0.04	−0.00	0.07	1.00		
U_0^+	0.17	−0.03	0.09	0.23	−0.09	−0.11	−0.04	0.11	−0.08	0.28	0.04	1.00	
$U_{-0}^{-,\mathrm{Im}}$	−0.02	0.17	−0.06	−0.01	0.35	0.06	0.01	0.00	0.01	−0.11	−0.27	−0.02	1.00
$U_{-0}^{-,\mathrm{Re}}$	0.01	−0.05	−0.05	−0.41	−0.09	0.01	0.01	0.03	0.02	0.02	0.11	−0.08	0.02
$U_{-0}^{+,\mathrm{Im}}$	−0.00	0.08	−0.16	−0.37	0.20	0.18	0.08	−0.09	0.10	−0.34	0.05	−0.41	0.18
$U_{-0}^{+,\mathrm{Re}}$	0.01	0.05	0.01	−0.07	0.05	−0.00	0.00	0.06	0.03	0.07	−0.00	−0.03	0.15
U_-^-	0.06	0.01	−0.01	−0.03	−0.02	−0.01	0.01	0.02	0.01	0.07	−0.01	−0.03	0.09
U_-^+	−0.05	−0.02	0.00	0.03	0.07	−0.02	−0.06	0.09	−0.05	0.05	−0.02	0.20	0.05
$U_{+0}^{-,\mathrm{Im}}$	0.08	0.12	−0.07	−0.17	0.07	0.10	0.09	0.02	0.09	−0.20	0.04	−0.24	0.04
$U_{+0}^{-,\mathrm{Re}}$	0.06	0.06	0.03	0.07	−0.13	−0.09	−0.15	0.09	0.00	0.20	0.09	0.04	−0.07
$U_{+0}^{+,\mathrm{Im}}$	−0.04	0.05	−0.13	−0.29	0.24	0.26	0.31	−0.32	0.09	−0.44	−0.06	−0.37	0.13
$U_{+0}^{+,\mathrm{Re}}$	0.07	0.02	−0.02	−0.11	0.04	0.11	0.23	−0.40	0.10	−0.20	−0.03	−0.21	0.02
$U_{+-}^{-,\mathrm{Im}}$	−0.05	−0.05	−0.01	0.07	−0.02	−0.07	−0.04	−0.03	−0.06	−0.09	−0.04	0.03	−0.02
$U_{+-}^{-,\mathrm{Re}}$	−0.06	0.01	−0.01	0.05	−0.03	−0.03	−0.02	0.07	−0.06	0.11	0.02	0.09	−0.00
$U_{+-}^{+,\mathrm{Im}}$	−0.04	−0.04	−0.01	0.06	−0.07	0.00	0.01	−0.06	0.06	−0.16	−0.04	−0.02	−0.05
$U_{+-}^{+,\mathrm{Re}}$	−0.10	−0.07	0.03	0.06	0.01	−0.04	−0.02	−0.07	0.03	−0.11	−0.07	−0.00	0.01
U_+^-	−0.04	0.03	0.01	0.04	−0.05	−0.05	−0.02	0.08	0.01	0.17	0.04	0.06	−0.03

	$U_{-0}^{-,\mathrm{Re}}$	$U_{-0}^{+,\mathrm{Im}}$	$U_{-0}^{+,\mathrm{Re}}$	U_-^-	U_-^+	$U_{+0}^{-,\mathrm{Im}}$	$U_{+0}^{-,\mathrm{Re}}$	$U_{+0}^{+,\mathrm{Im}}$	$U_{+0}^{+,\mathrm{Re}}$	$U_{+-}^{-,\mathrm{Im}}$	$U_{+-}^{-,\mathrm{Re}}$	$U_{+-}^{+,\mathrm{Im}}$	$U_{+-}^{+,\mathrm{Re}}$	U_+^-
$U_{-0}^{-,\mathrm{Re}}$	1.00													
$U_{-0}^{+,\mathrm{Im}}$	0.25	1.00												
$U_{-0}^{+,\mathrm{Re}}$	0.25	0.12	1.00											
U_-^-	0.17	0.04	0.07	1.00										
U_-^+	0.01	0.09	0.04	−0.13	1.00									
$U_{+0}^{-,\mathrm{Im}}$	0.04	0.24	0.00	0.01	−0.07	1.00								
$U_{+0}^{-,\mathrm{Re}}$	0.09	−0.04	0.08	0.05	−0.00	0.26	1.00							
$U_{+0}^{+,\mathrm{Im}}$	0.01	0.40	−0.04	−0.02	−0.08	0.32	−0.14	1.00						
$U_{+0}^{+,\mathrm{Re}}$	−0.03	0.09	−0.02	0.02	−0.26	0.17	−0.09	0.35	1.00					
$U_{+-}^{-,\mathrm{Im}}$	−0.12	−0.19	−0.10	−0.11	−0.03	−0.05	−0.07	−0.04	0.03	1.00				
$U_{+-}^{-,\mathrm{Re}}$	0.04	−0.05	0.03	0.12	0.09	−0.05	0.08	−0.09	−0.12	−0.01	1.00			
$U_{+-}^{+,\mathrm{Im}}$	−0.09	−0.17	−0.13	−0.03	−0.10	−0.02	−0.05	−0.04	0.08	0.35	−0.02	1.00		
$U_{+-}^{+,\mathrm{Re}}$	−0.13	−0.19	−0.10	−0.03	−0.04	−0.07	−0.15	0.01	0.07	0.25	−0.01	0.18	1.00	
U_+^-	0.06	0.02	0.05	−0.03	0.14	0.11	0.30	−0.09	−0.13	−0.03	0.16	−0.10	−0.11	1.00

Table 6: Correlation matrix of statistical uncertainties for the U and I coefficients. Note that all elements above the diagonal are omitted for readability.
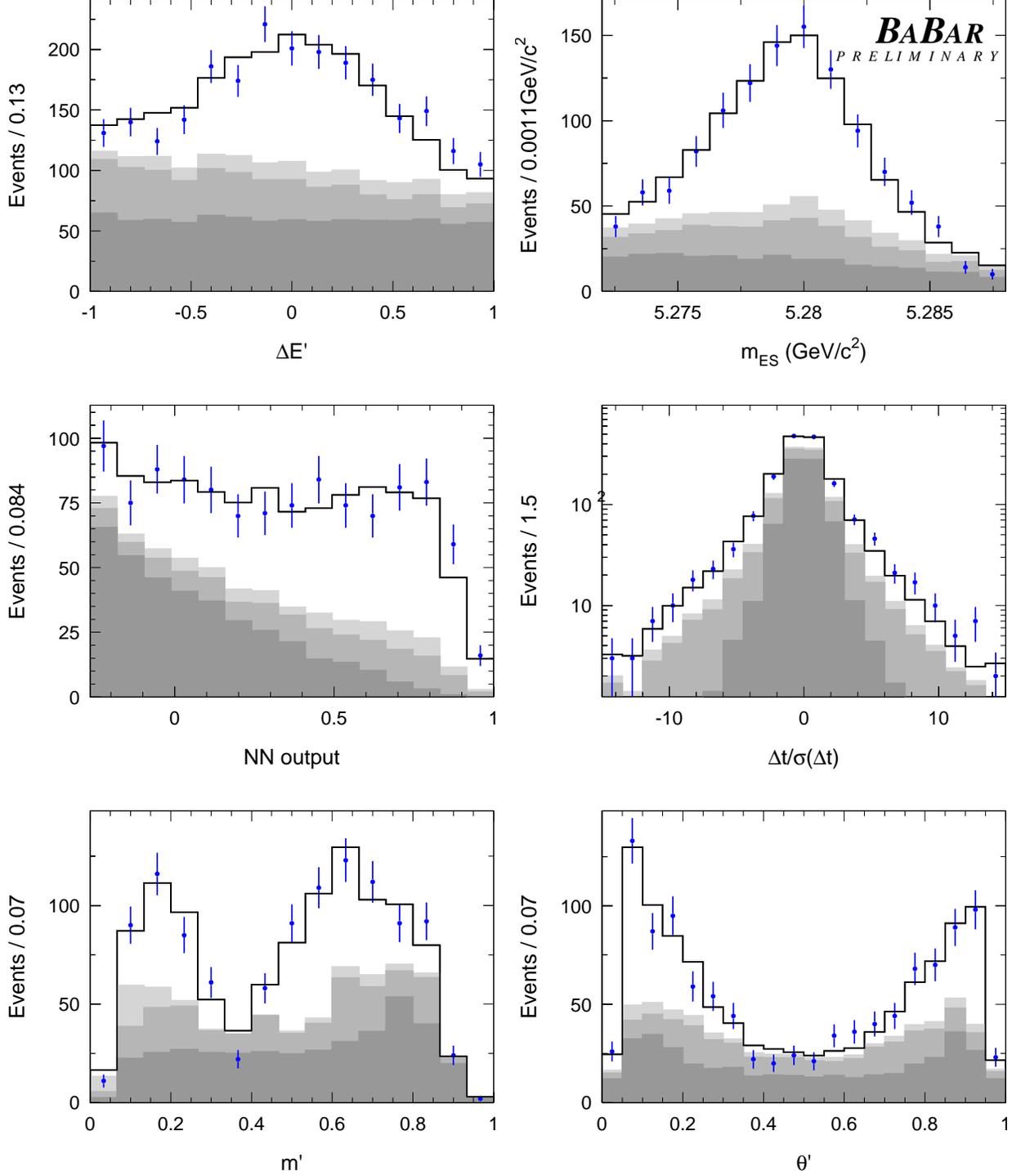
Figure 3: Distributions of (top to bottom, left to right) $\Delta E'$, m_{ES}, NN output, $\Delta t/\sigma(\Delta t)$, m' and θ' for samples enhanced in $B^0 \to \pi^+\pi^-\pi^0$ signal. The dots with error bars give the on-resonance data. The solid histogram shows the projection of the fit result. The dark, medium and light shaded areas represent respectively the contribution from continuum events, the sum of continuum events and the B-background expectation, and the sum of these and the misreconstructed signal events.
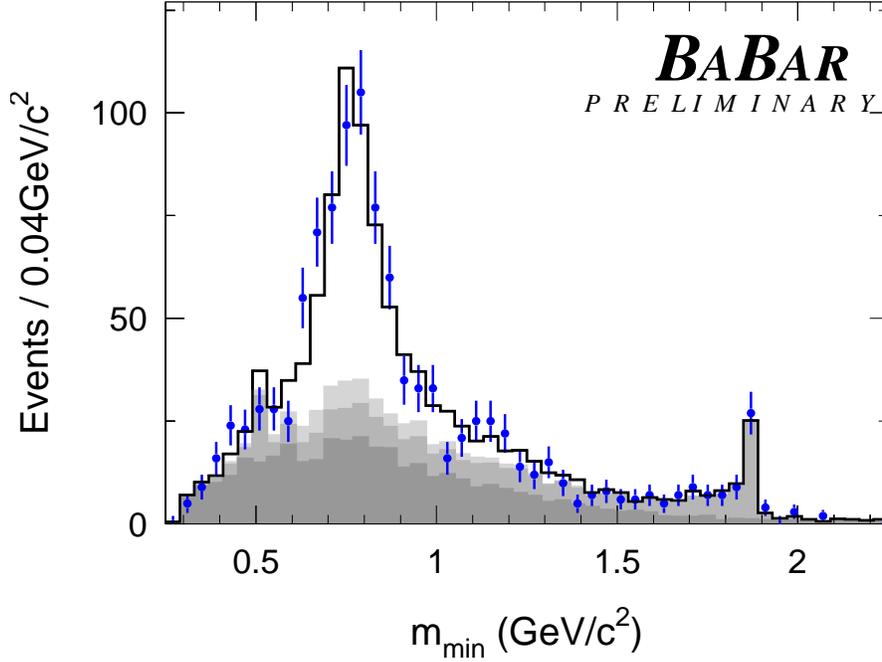
Figure 4: Distribution of minimum of the three di-pion invariant masses, for samples enhanced in $B^0 \to \pi^+\pi^-\pi^0$ signal. The dots with error bars give the on-resonance data. The solid histogram shows the projection of the fit result. The dark, medium and light shaded areas represent respectively the contribution from continuum events, the sum of continuum events and the B-background expectation, and the sum of these and the misreconstructed signal events.

	$\mathcal{A}_{\rho\pi}$	C	ΔC	S	ΔS
$\mathcal{A}_{\rho\pi}$	1.93				
C	-0.71	9.68			
ΔC	-0.55	2.63	8.93		
S	-0.03	-0.71	-0.13	15.3	
ΔS	-0.03	-0.57	-0.07	3.93	17.08

Table 7: Covariance matirx multipled by 1000 of the quasi-two-body parameters.
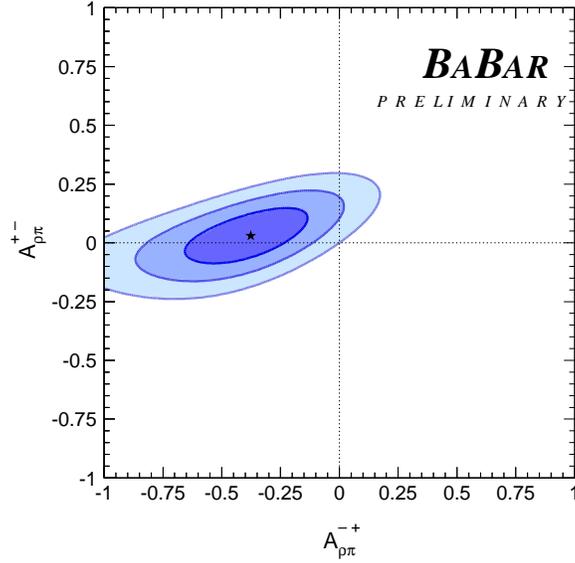
Figure 5: Confidence level contours for the direct CP asymmetries $\mathcal{A}_{\rho\pi}^{+-}$ versus $\mathcal{A}_{\rho\pi}^{-+}$. The shaded areas represent 1σ, 2σ and 3σ contours, respectively.
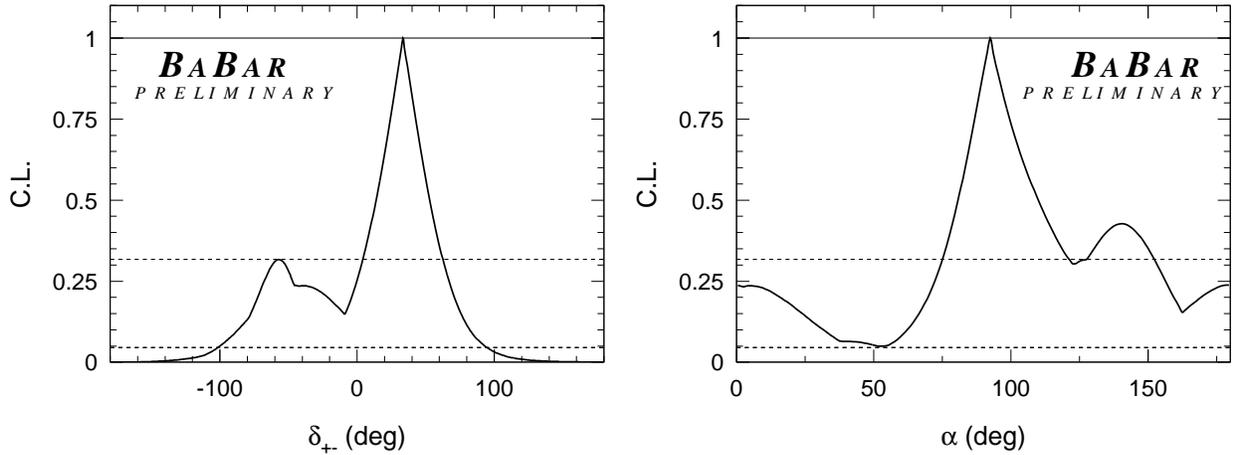

Figure 6: Confidence level functions for δ_{+-} (left) and α (right). Indicated by the dashed horizontal lines are the confidence level (C.L.) values corresponding to 1σ and 2σ, respectively.